



Computational Mechanics  
Research and Support  
for Aerodynamics and Hydraulics  
at TFHRC

**About Argonne National Laboratory**

Argonne is a U.S. Department of Energy laboratory managed by UChicago Argonne, LLC under contract DE-AC02-06CH11357. The Laboratory's main facility is outside Chicago, at 9700 South Cass Avenue, Argonne, Illinois 60439. For information about Argonne and its pioneering science and technology programs, see [www.anl.gov](http://www.anl.gov).

**Availability of This Report**

This report is available, at no cost, at <http://www.osti.gov/bridge>. It is also available on paper to the U.S. Department of Energy and its contractors, for a processing fee, from:

U.S. Department of Energy  
Office of Scientific and Technical Information  
P.O. Box 62  
Oak Ridge, TN 37831-0062  
phone (865) 576-8401  
fax (865) 576-5728  
[reports@adonis.osti.gov](mailto:reports@adonis.osti.gov)

**Disclaimer**

This report was prepared as an account of work sponsored by an agency of the United States Government. Neither the United States Government nor any agency thereof, nor UChicago Argonne, LLC, nor any of their employees or officers, makes any warranty, express or implied, or assumes any legal liability or responsibility for the accuracy, completeness, or usefulness of any information, apparatus, product, or process disclosed, or represents that its use would not infringe privately owned rights. Reference herein to any specific commercial product, process, or service by trade name, trademark, manufacturer, or otherwise, does not necessarily constitute or imply its endorsement, recommendation, or favoring by the United States Government or any agency thereof. The views and opinions of document authors expressed herein do not necessarily state or reflect those of the United States Government or any agency thereof, Argonne National Laboratory, or UChicago Argonne, LLC.

# **Computational Mechanics Research and Support for Aerodynamics and Hydraulics at TFHRC, Year 3 Quarter 3 Progress Report**

---

by

S.A. Lottes<sup>1</sup>, C. Bojanowski<sup>1</sup>, C.A. Robeck<sup>1</sup>, J. Shen<sup>2</sup>, and Z. Xie<sup>2</sup>

<sup>1</sup> Transportation Research and Analysis Computing Center (TRACC)

Energy Systems Division, Argonne National Laboratory

<sup>2</sup> Turner-Fairbank Highway Research Center

submitted to

Kornel Kerenyi<sup>1</sup> and Harold Bosch<sup>1</sup>

<sup>1</sup> Turner-Fairbank Highway Research Center

October 2013

# Table of Contents

1. Introduction and Objectives .....	7
1.1. Hydraulics Modeling and Analysis Summary .....	8
1.2. Wind Engineering Modeling and Analysis Summary .....	8
1.3. Technology Transfer and Facility and User Support .....	9
2. Hydraulics Modeling and Analysis .....	10
2.1. Modeling of Flow through Grates.....	10
2.1.1. Model Development .....	10
2.1.2. Results .....	12
2.2. Onset of Rip-Rap Motion using STAR-CCM+ Coupled with LS-DYNA.....	17
2.3. Composite Manning’s n of Fish Passage Culvert at TFHRC.....	24
3. Wind Engineering Modeling and Analysis.....	31
3.1. Drag and Lift on Variable Message Signs under Conditions with Wind.....	31
3.1.1. Model Development .....	31
3.1.2. Results .....	32
3.2. Wind Tunnel Model with Neutral Vane Position in Turbulence Generator .....	36
4. Technology Transfer and TRACC Facility User Support .....	40

## List of Figures

Figure 2.1 Grate design with vanes.....	10
Figure 2.2 Surface Representation of R-3210-L Grate with Vanes (Flow in +X-Direction) .....	11
Figure 2.3 Model of Sloped Street with Grate R-3210-L.....	11
Figure 2.4 Volume Fraction of Water (Red) Around Vein Style Grate .....	13
Figure 2.5 Streamlines of Flow Around Vein Style Grate.....	14
Figure 2.6 Multi-Component Flow at Inlet With: Air (Red), Water, (Blue), and Tracer (Green).....	14
Figure 2.7 Single water fluid flow over and through the grate.....	15
Figure 2.8 Two water fluid flow over grate with front water in blue and side water in green .....	16
Figure 2.9 A stone surface and feature curves created on all edges of the mesh.....	17
Figure 2.10 Current implementation of coupling workflow between STAR-CCM+ and LS-DYNA.....	18
Figure 2.11 Geometry of the CFD model (a) layout 1, side view (b) layout 1, top view (c) layout 2, top view.....	21
Figure 2.12 Snapshots from simulation for layout 1 and inlet velocity of 3.0 m/s.....	23
Figure 2.13 Snapshots from simulation for layout 2 and inlet velocity of 3.0 m/s.....	24
Figure 2.14 Force Analysis Sketch on the Culvert Pipe .....	25
Figure 2.15 Geometrical Parameters of Culvert .....	26
Figure 2.16 Geometrical Model with Uniform Bed Roughness of $D_{50}$ .....	27
Figure 2.17 Pressure distribution on two planes with periodic boundary .....	27
Figure 2.18 Pressure difference monitor between two planes with periodic boundaries.....	28
Figure 2.19 Velocity magnitude distribution .....	28
Figure 2.20 Velocity Magnitude Distribution on the Cross Section.....	29
Figure 2.21 Analysis of Regression between Manning' n and $\lg(\text{Re})$ .....	30
Figure 2.22 Linear Regression between Manning' n and $\delta/R_H$ .....	30
Figure 3.1 Initial Sign Geometry.....	32

Figure 3.2 Drag and Lift Coefficients As a Function of Y-Axis Angle of Attack.....	33
Figure 3.3 Pressure distribution around sign (left) perpendicular to the flow and (right) rotated 30 about Z axis.....	33
Figure 3.4 Drag and Lift Coefficients as a Function of Z-Axis Angle of Attack .....	34
Figure 3.5 Pressure distribution around sign (left) rotated -10 deg (CCW) and (right) +5 deg (CW) about X axis .....	34
Figure 3.6 Pressure Distribution Around Sign With Mesh Aligned With Flow, three meshing schemes ...	35
Figure 3.7 CFD computed velocity field at the height of the laboratory measurements with measurement cross sections .....	36
Figure 3.8 Comparison of measured and computed velocity distribution at first column of points that spanned the room.....	37
Figure 3.9 Comparison of measured and computed velocity distribution at the second set of measured points spanning the room in the downstream of the wind tunnel jet .....	37
Figure 3.10 Comparison of measured and computed velocity distribution at the third set of measured points spanning the room in the downstream of the wind tunnel jet .....	38
Figure 3.11 Comparison of measured and computed velocity distribution at the fourth set of measured points spanning the room in the downstream of the wind tunnel jet .....	38
Figure 3.12 Measured and CFD velocity magnitude near the wall with the door .....	39
Figure 3.13 Measured and CFD velocity magnitude near the wall with the turbulence generator .....	39

## List of Tables

Table 2.1 Geometry and Flow Parameters for Grate Simulation .....	12
Table 2.2 Results of Single Fluid and Two Fluid Water Flow Over Grate with Vanes .....	16
Table 2.3 Motion of the Rocks in a Specific Analyzed Case .....	22
Table 3.1 Meshing Schemes.....	32
Table 3.2 Drag and Lift Coefficients for Each Meshing Scheme .....	35

## **1. Introduction and Objectives**

The computational fluid dynamics (CFD) and computational structural mechanics (CSM) focus areas at Argonne's Transportation Research and Analysis Computing Center (TRACC) initiated a project to support and compliment the experimental programs at the Turner-Fairbank Highway Research Center (TFHRC) with high performance computing based analysis capabilities in August 2010. The project was established with a new interagency agreement between the Department of Energy and the Department of Transportation to provide collaborative research, development, and benchmarking of advanced three-dimensional computational mechanics analysis methods to the aerodynamics and hydraulics laboratories at TFHRC for a period of five years, beginning in October 2010. The analysis methods employ well benchmarked and supported commercial computational mechanics software. Computational mechanics encompasses the areas of Computational Fluid Dynamics (CFD), Computational Wind Engineering (CWE), Computational Structural Mechanics (CSM), and Computational Multiphysics Mechanics (CMM) applied in Fluid-Structure Interaction (FSI) problems.

The major areas of focus of the project are wind and water effects on bridges — superstructure, deck, cables, and substructure (including soil), primarily during storms and flood events — and the risks that these loads pose to structural failure. For flood events at bridges, another major focus of the work is assessment of the risk to bridges caused by scour of stream and riverbed material away from the foundations of a bridge. Other areas of current research include modeling of the salt spray transport into bridge girders to address suitability of using weathering steel in bridges, CFD analysis of the operation of the wind tunnel in the TFHRC wind engineering laboratory, and coupling of CFD and CSM software to solve fluid structure interaction problems, primarily analysis of bridge cables in wind and stability of large riprap as a countermeasure for bridge scour.

This quarterly report documents technical progress on the project tasks for the period of April through June 2013.

## **1.1. Hydraulics Modeling and Analysis Summary**

The primary Computational Fluid Dynamics (CFD) activities during the quarter in hydraulics were in the areas of analysis of flow through street grates, coupled fluid structure interaction of flow around large rip-rap rocks to determine the onset of motion of one or more rocks, and determination of a composite Manning's n using CFD for fully developed flow through a culvert with corrugated walls and gravel on the bottom.

The street grate flow model was extended by placing one of the drain geometries in a street with cross slope and a longitudinal slope. A method to determine the fraction of flow intercepted by the drain from the side was also investigated. In this method the flow aligned with the side of the grate and the flow aligned with the front of the grate are defined as two separate immiscible fluids. This setup allows the amount of water coming from each source to be calculated at the drain exit. Details are presented in Section 2.1

The procedures for coupling CFD analysis using STAR-CCM+ and ridged body motion and collisions of rip-rap rocks using LS-DYNA were completed and tested on a bed with a large number of rocks with three rocks in the rock layer that could move. Previous problems with the rock geometry being severely distorted after numerous remeshing operations in the CFD domain as rocks move were solved by generating numerous feature curves on the rock surfaces. Feature curves are geometry entities that the STAR-CCM+ mesh generator will keep fixed when generating the mesh. They are often used to maintain sharp edges or corners where those may be important for the CFD computation. Details of the automated FSI coupling between STAR-CCM+ and LS-DYNA for analysis of onset of rip-rap motion from the detail pressure distribution on the rocks and interactions with surrounding rocks are provided in Section 2.2

A procedure to use CFD to determine a composite Manning's n value accounting for the specific energy losses from different types of roughness elements in a culvert was developed for fully developed flow conditions. The different roughness elements were the culvert corrugations and gravel in the bottom of the culvert. A parametric series of CFD computations was run and the results were used to determine a relation between the Manning's n value and the culvert pipe geometry, embedment, and gravel particle size. The details of this work are found in Section 2.3. The procedure and relation are being applied to the development of new design procedures for culvert applications that allow for fish passage.

## **1.2. Wind Engineering Modeling and Analysis Summary**

The primary CFD activities during the quarter in wind engineering focused on further analysis of aerodynamic characteristics and behavior of Variable Message Signs (VMS), and analysis of flow quality in the Turner-Fairbank's wind tunnel lab. Lift and drag coefficients of the VMS were studied in detail for different angles of attack of the wind. The details of that study are covered in Section 3.1.

In the previous models of the wind tunnel laboratory the vanes of the turbulence generator weren't in their neutral position i.e. they were turned and were creating a blockage in the returning flow on one

side of the tunnel. A new geometry was imported and some of the flow characteristics were compared between the old and the updated model. The details of this update are described in Section 3.2.

### **1.3. Technology Transfer and Facility and User Support**

The biweekly CFD collaborator videoconferences with TRACC staff, Turner-Fairbank Highway Research Laboratory staff, and university and DOT researchers were continued through the quarter. CFD technical support for TRACC cluster users was also continued.

## 2. Hydraulics Modeling and Analysis

### 2.1. Modeling of Flow through Grates

#### 2.1.1. Model Development

Work on modeling procedures for a parametric study of intercepted flow through street drain grates of varying designs was continued. Previously, a model for flow through grates in a flat domain was built and tested [1], and a model for flow down a sloped street with a cross slope was built and tested [2]. In this quarter these models were combined, and a method to determine the fraction of the flow intercepted by a grate that comes from the street side of the grate was developed.

One of the grate geometries of interest to Minnesota DOT was used based on the Neenah grate catalog [3] as shown in Figure 2.1.

#### **R-3210-L** Catch Basin Frame, Grate

Heavy Duty

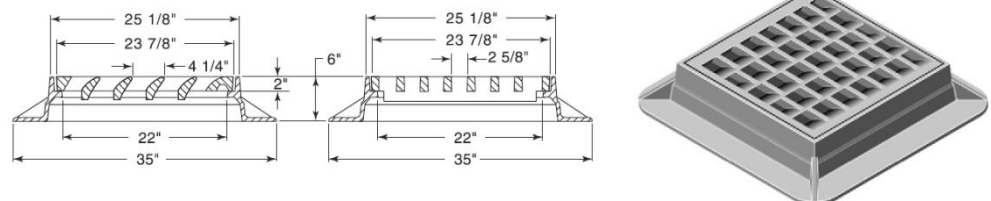


Figure 2.1 Grate design with vanes

Files containing the grate geometry were imported into STAR-CCM+ and combined with the street model geometry. The R-3210-L grate employs vanes in the grate openings to capture a larger fraction of the runoff. The surface geometry of this grate is shown in Figure 2.2, and the geometry model of the grate in a sloped street is shown in Figure 2.3. The model extends in the cross street direction from the curb to the spread width of water. The height above street level at the thin part of the inlet cross section on the left allows space for the air above the water free surface in the model.

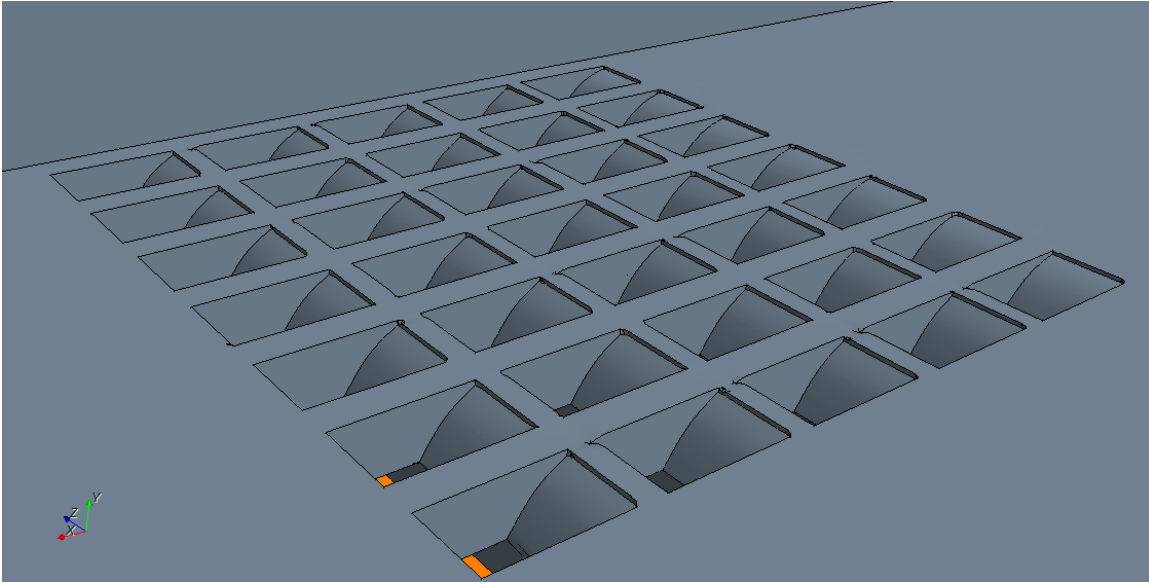


Figure 2.2 Surface Representation of R-3210-L Grate with Vanes (Flow in +X-Direction)

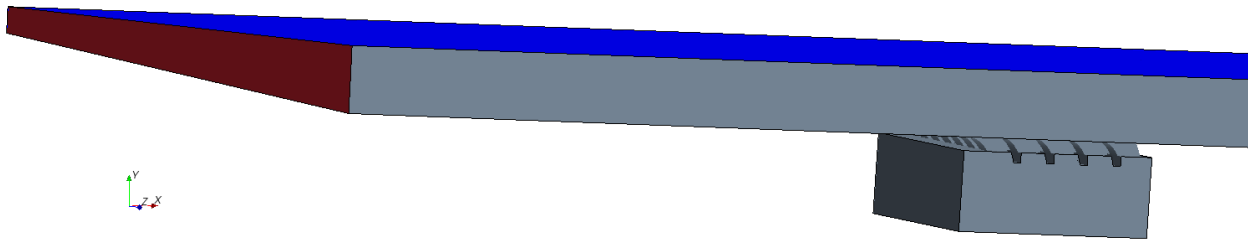


Figure 2.3 Model of Sloped Street with Grate R-3210-L

The CFD solver requires the velocity at the inlet at the upstream section of the street, the red quadrilateral on the left side of Figure 2.3. The volume rate of flow is determined from the street geometry, the water spread,  $T$ , and Manning  $n$  value from HEC 22, Equation 4-2 [2]:

$$Q = \left( \frac{K_u}{n} \right) S_x^{1.67} S_L^{0.5} T^{2.67} \quad 2.1$$

where  $Q$  is the volume flow rate,  $K_u$  a constant,  $n$  is the Manning's roughness coefficient,  $S_x$  is the street cross slope,  $S_L$  is the street longitudinal slope, and  $T$  is the width of the water surface. The values of the parameters and the calculated flow rate,  $Q$ , are given in Table 2.1. The area of the portion of the inlet with water flowing is  $A = (\frac{1}{2} S_x T^2) = 0.148 \text{ m}^2$  ( $1.6 \text{ ft}^2$ ). The average velocity at the inlet is then  $Q/A = 2.8 \text{ m/s}$  ( $9.2 \text{ ft/s}$ ) is set as the inlet boundary condition for the water. The curb, grate, and catch basin sides are all set as wall boundaries. The top of the domain is set as a pressure boundary to allow air to escape

or enter as needed to compensate for changes in the water free surface level. The downstream exit boundary at the street level and the bottom of the modeled section of the catch basin are set as pressure boundaries. The pressure at the bottom of the catch basin is set to atmospheric to allow water to fall freely through it. The pressure at the street section outflow boundary is set to the value at the cell centroids adjacent to the outflow boundary. This boundary setting accounts for the back pressure of water just downstream of the street level exit boundary.

**Table 2.1 Geometry and Flow Parameters for Grate Simulation**

Flow Parameter	Value (metric)	Value (English)
<b>Q</b>	0.422 (m <sup>3</sup> /s)	15 ft <sup>3</sup> /s
<b>K<sub>u</sub></b>	0.376	0.56
<b>n</b>	0.015	0.015
<b>S<sub>x</sub></b>	0.05	0.05
<b>S<sub>L</sub></b>	0.05	0.05
<b>T</b>	2.44 (m)	8 (ft)

### 2.1.2. Results

The two parameters of primary interest in the analysis results are the fraction of the flow intercepted by the grate and the fraction of the intercepted flow coming from the water passing the cross street side of the grate. The total flow intercepted by the grate is easy to calculate by integrating the water mass flux over the grate outlet and dividing by the density of water. The fraction coming from the side of the grate that is diverted by the grate into the catch basin, however is not easy to calculate. Figure 2.4 shows the water levels at the front of the grate on the left, the dropping level along the side, and the level at the downstream side as a water volume fraction. It also contains a visualization of the free surface and water volume fractions on catch basin boundaries. The amount of water flow from the side entering over the grate can be computed, but there is no simple way to calculate how much of that is captured by the grate and how much passes over the grate and continues down the street.

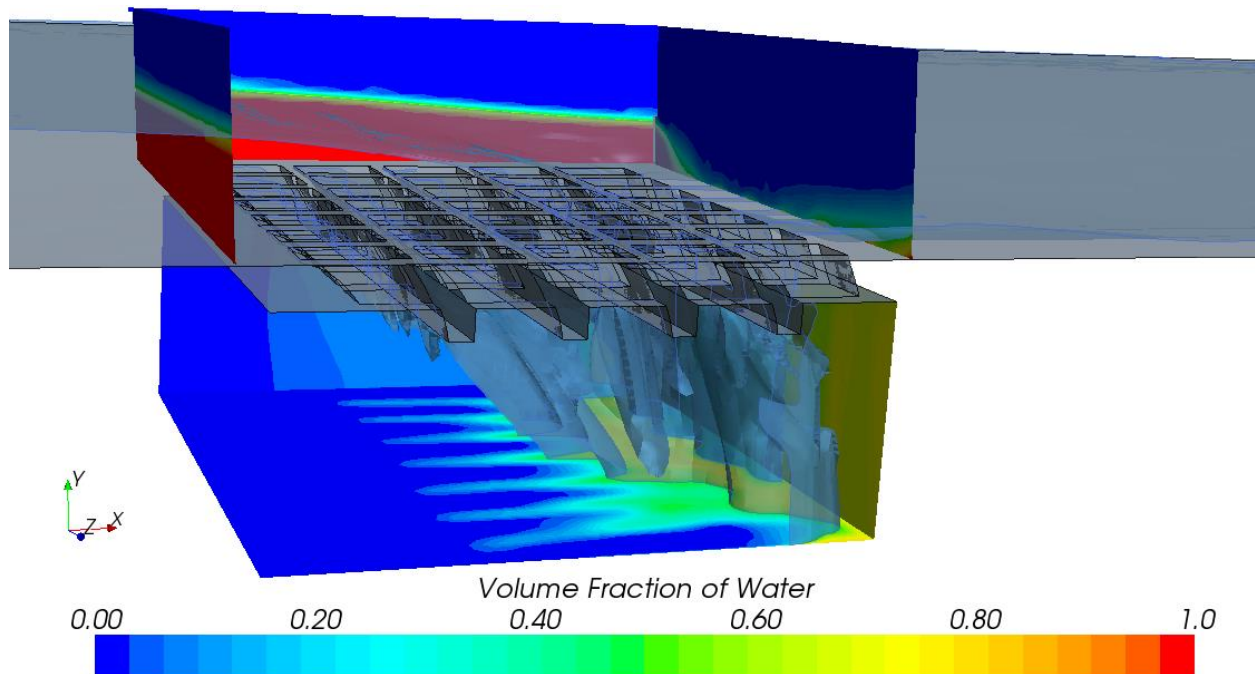


**Figure 2.4 Volume Fraction of Water (Red) Around Vein Style Grate**

Plotting streamlines, as in Figure 2.5 provides a visualization that clearly shows flow from the side of the grate passing through the grate into the catch basin and provides a qualitative view of the partial region on the grate opening that is capturing flow from the side, but a quantitative measure of the amount of flow from the side entering the catch basin is not available with this approach.

Adding a passive scalar, which can be thought of as a dye, to the flow entering in line with the side of the grate, and then computing the fraction of the passive scalar captured by the grate was tried and did not yield physically reasonable results. The approach involves solving an additional partial differential equation for the concentration of the passive scalar quantity. The scalar quantity can and was given the properties of water, and in this case almost no molecular diffusion and very little turbulent diffusion would be expected between the inlet and the grate. However, a large amount of non-physical numerical diffusion was observed when this approach was tested, and consequently the results were not sufficiently accurate.

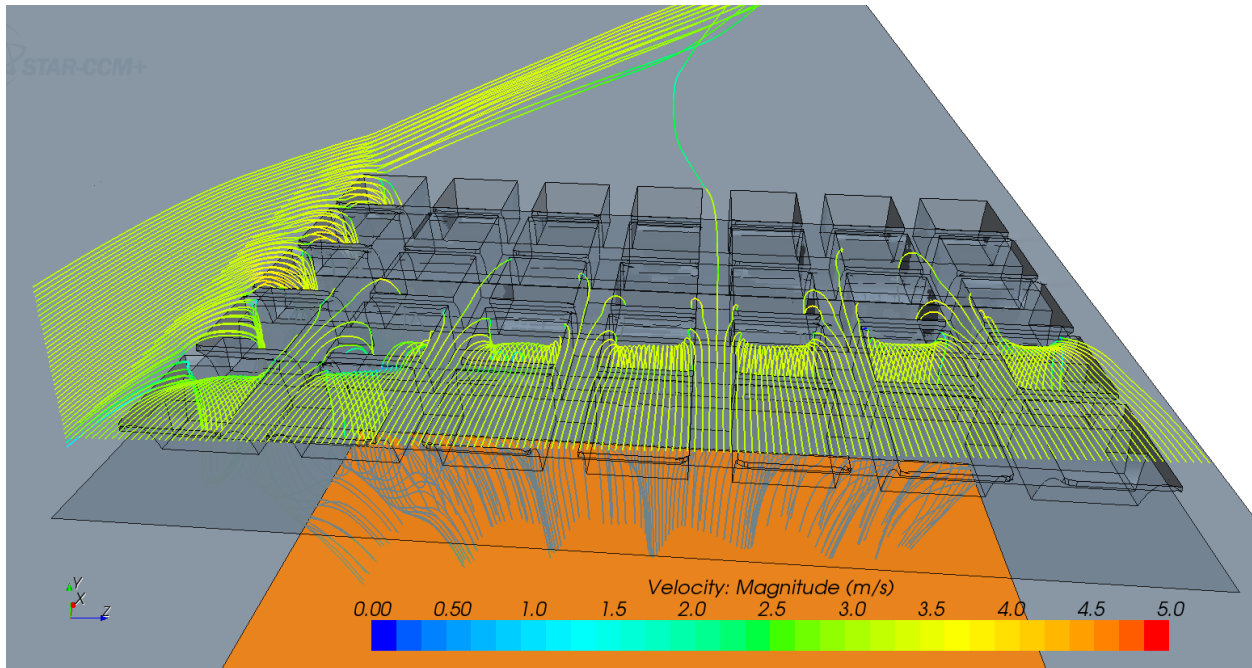


**Figure 2.5 Streamlines of Flow Around Vein Style Grate**

The VOF physics model in STAR-CCM+ allows for an arbitrary number of immiscible fluids to be defined in the flow field. This capability was used to develop a method to calculate the amount of side flow intercepted by a grate to engineering accuracy. Two different fluids were defined with the properties of water. One of these is water that enters the domain flowing down the street in line with and to the side of the grate, as shown in the green region in Figure 2.6. The blue area of the inlet in Figure 2.6 is a second fluid water that enters inline to flow over the top of the grate. Because these two fluids are treated as immiscible by the physics solver, the numerical diffusion of the passive scalar approach is avoided. The red area in Figure 2.6 is the zone where air enters the domain. The thin green layer sandwiched between the blue and red is not side water, rather it is just the result of color interpolation in the row of cells where the blue water and air meet.

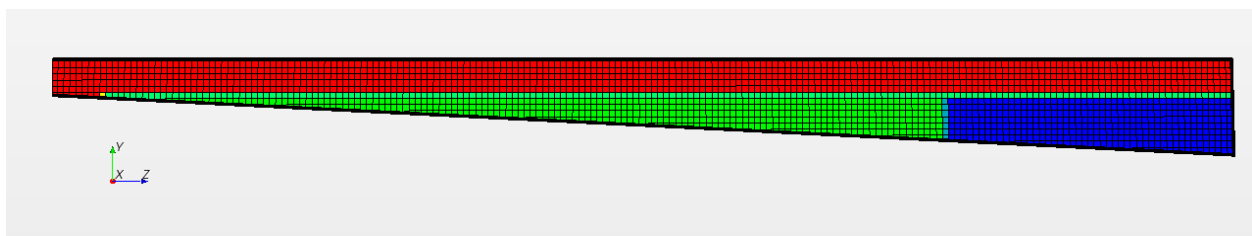


**Figure 2.6 Multi-Component Flow at Inlet With: Air (Red), Water, (Blue), and Tracer (Green)**

In reality the two types of water, that entering to the side of the grate and that entering inline to flow over the grate are not immiscible and therefore, computations were done with a single water fluid in the system and with the two water fluids. The solutions were compared to see how much difference there is in using the two fluid approach to calculate the amount of side water flow through the grate.

Figure 2.7 shows a visualization of the free surface with air and only one water fluid in the system. A large fraction of water entering over the grate is captured leaving some patches of dry street just downstream of several of the last row of grate openings. The contour of deeper water flowing toward the curb side to the right is also visible.

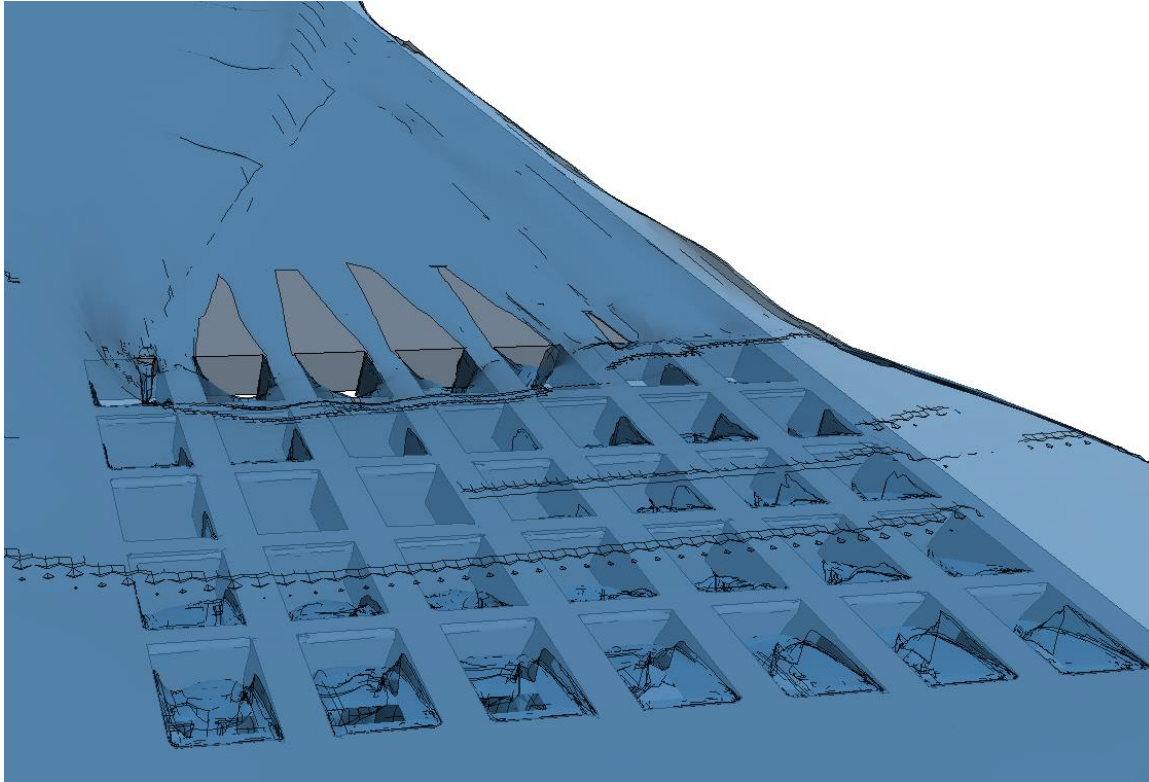


**Figure 2.7 Single water fluid flow over and through the grate**

Figure 2.8 shows a visualization of the free surface of a case with the same flow conditions as that in Figure 2.7, but with two immiscible water fluids, green water approaching the grate from the side and blue water approaching the grate from the front. Because the grate captures a large fraction of water approaching from the front, its level drops and the green side water begins to spread toward the curb, even before the grate is reached. The green side water can be seen flowing into the outermost column of grate holes along with the blue water. There is a small sliver of dry street downstream of the grate between the green and blue water due to the surface tension and the fact that they are immiscible. The small gap between shallow blue and deeper green water is eventually closed in the downstream as the green water flows toward the curb to bring the water level back to uniform.

Table 2.2 shows quantitative results of flow diverted by the grate for the single and two fluid water flow cases. The total flow diverted into the catch basin for these models matches to approximately 3 digits with a difference of less than one percent. For the single water fluid case 40.3 percent of the inflow is diverted by the grate, while for the two immiscible liquid fluid case about a half percent more, 40.5 percent, is diverted. Therefore, using the two immiscible liquid fluids model to determine the amount of

flow entering the grate from the side appears to be adequate for engineering use. About 5.3 percent of the water diverted by the grate was from side water.

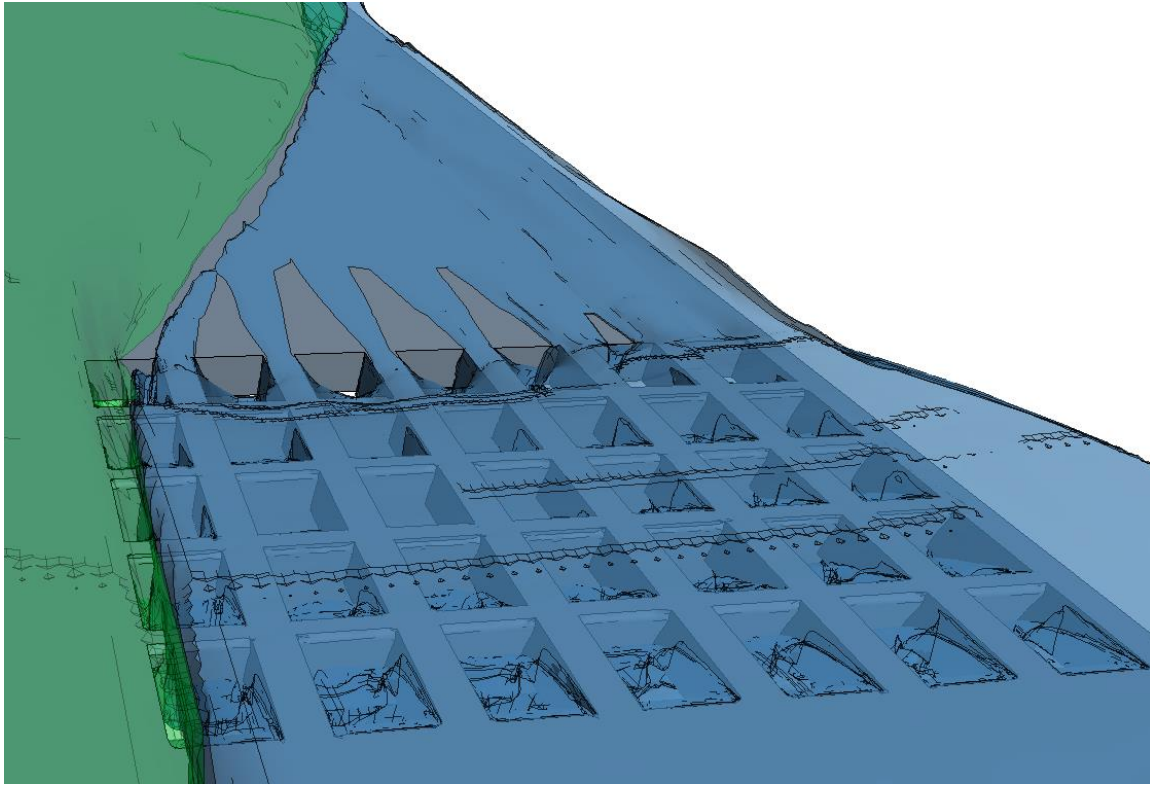


Figure 2.8 Two water fluid flow over grate with front water in blue and side water in green

Table 2.2 Results of Single Fluid and Two Fluid Water Flow Over Grate with Vanes

Flow Parameter	Value (metric) m <sup>3</sup> /s	Value (English) ft <sup>3</sup> /s	Percent
$Q_{in}$	0.422	14.9	100%
$Q_{grate}$ single water fluid model	0.170	6.00	40.3% of $Q_{in}$
$Q_{grate}$ two water fluid model	0.171	6.04	40.5% of $Q_{in}$
$Q_{grate\_side}$	0.009	0.32	5.3% of $Q_{grate}$ 2.2% of $Q_{in}$

[1] S.A. Lottes, C. Bojanowski, J. Shen, and Z.Xie, Computational Mechanics Research and Support for Aerodynamics and Hydraulics at TFHRC, Year 2 Quarter 4 Progress Report, Argonne National Laboratory, Report ANL/ESD/12-14, November, 2012.

[2] S.A. Lottes, C. Bojanowski, J. Shen, and Z.Xie, Computational Mechanics Research and Support for Aerodynamics and Hydraulics at TFHRC, Year 3 Quarter 1 Progress Report, Argonne National Laboratory, Report ANL/ESD/13-2, May, 2013.

[3] Neenah Foundry, <http://www.nfco.com/municipal/products/combination-inlets/without-curb-box/r-3210-g>

[4] Hydraulic Engineering Circular No. 22, Third Edition, Urban Drainage Design Manual, FHWA-HHI-10-009, Federal Highway Administration, September 2009.

## 2.2. Onset of Rip-Rap Motion using STAR-CCM+ Coupled with LS-DYNA

Work on modeling the onset of rip-rap motion continues with the improvements to the procedure developed in previous quarter. The issue with volume mesher that was distorting the boundaries of the stone was solved by creating and imposing on each time step feature curves on each edge of the stone NASTRAN surface. An example of imported stone surface and feature curves retrieved in Star-CCM+ is shown in Figure 2.9.

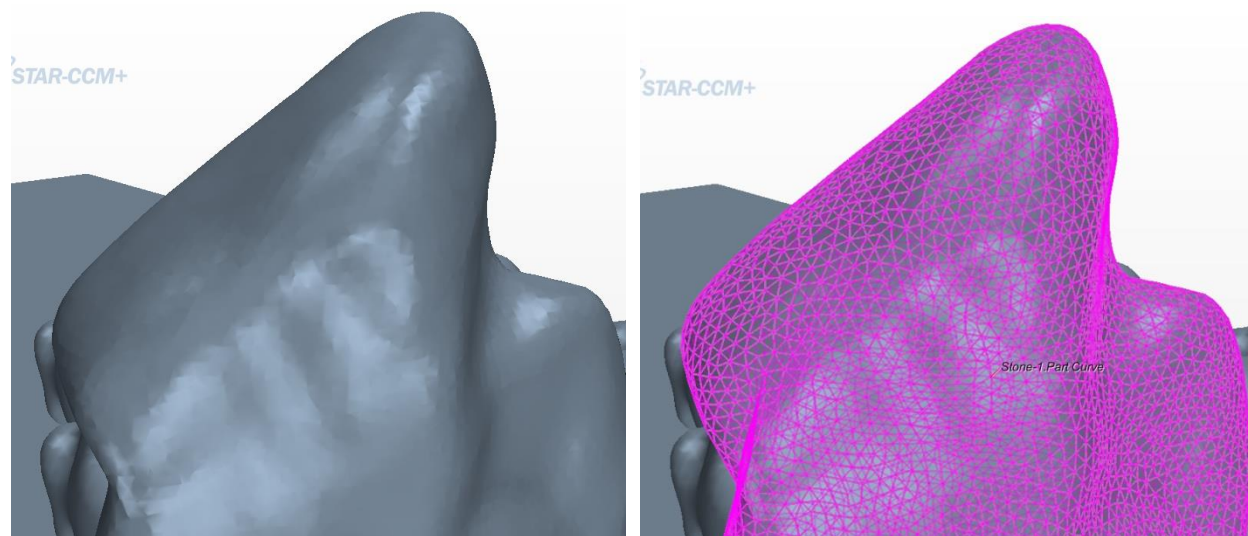


**Figure 2.9 A stone surface and feature curves created on all edges of the mesh**

Once this obstacle was solved the whole process was automated. Figure 2.10 presents the current workflow of the procedure to analyze incipient motion of riprap for a given arrangement and flow velocity. The procedure is executed in a LINUX environment with a control program written in the

Python language. The program starts execution of needed components of LS-DYNA and STAR-CCM+, including the solvers and meshing software, and LS-PREPOST (LS-DYNA pre- and post-processing software). It also translates output files into a neutral NASTRAN format recognized by both software packages.

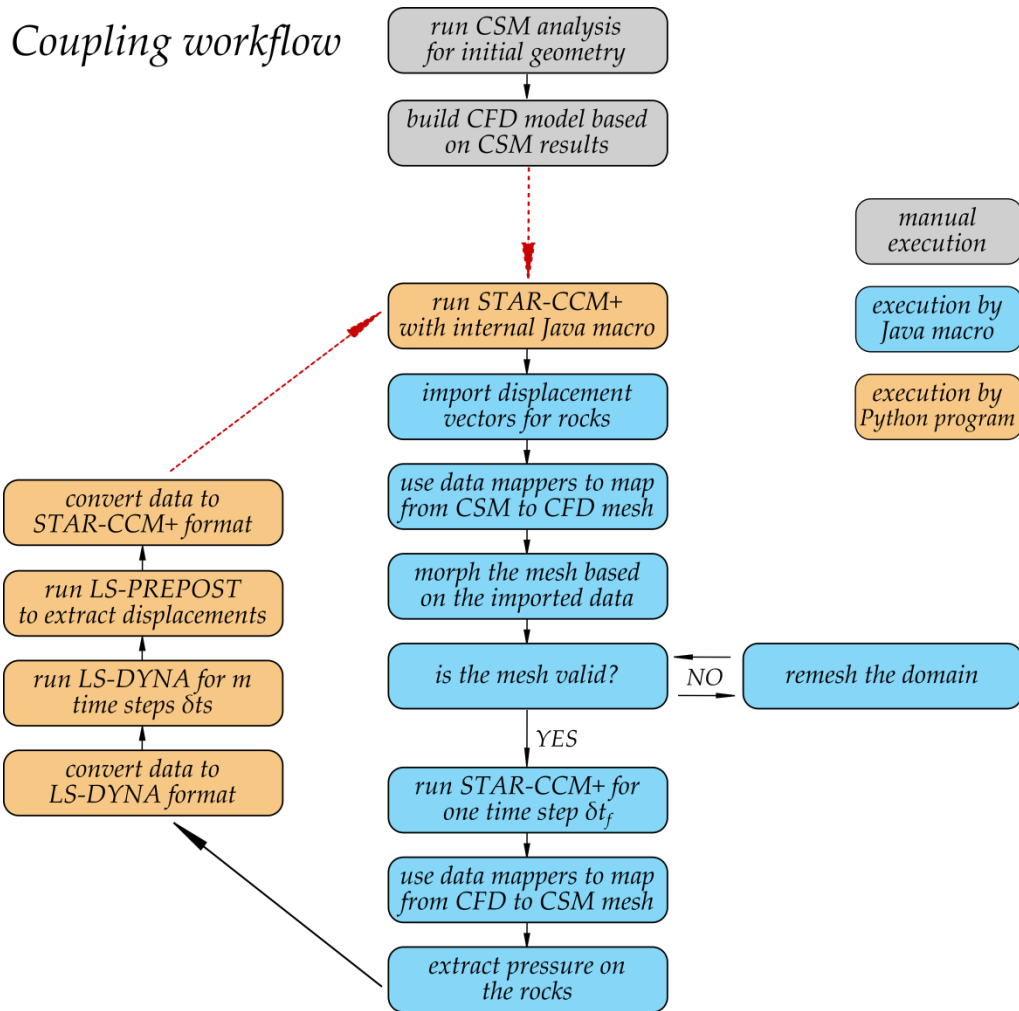


**Figure 2.10** Current implementation of coupling workflow between STAR-CCM+ and LS-DYNA

The analysis procedure begins with initialization runs in both solvers started manually. The LS-DYNA run provides the initial position of the rocks under gravity loading. This position is used as a basis for CFD domain geometry. The CFD model is run until pseudo steady state conditions are achieved with all rocks stationary. Subsequently the Python program is started. Execution of the CFD part is quite complex and requires an internal Java macro to run within STAR-CCM+ to import rock displacements and map them from the CSM mesh to the CFD mesh and vice versa. It is almost always the case that the resolution between the fluid and structural grids is different, especially when two separate solvers are handling the fluid and solid domains. STAR-CCM+ provides accurate data mappers for non-conforming meshes [1]. This mapping has to be performed at each time step as the underlying mesh deforms. The

displacements of the body are distributed throughout the morphed fluid domain to maintain cell quality. No cells are added or removed in the morphing process and their neighbor relationships are preserved so the mesh topology remains constant. The Arbitrary Lagrangian-Eulerian (ALE) algorithm is invoked to solve transport equations resulting from the moving underlying mesh [1, 2]. It allows for retaining exact shape of the interface between the solid and the fluid. The mesh morpher is a sophisticated algorithm that yields a high quality mesh in the whole computational domain based on the initial mesh and the displacement of the boundaries. However, in cases where the displacement of a rock becomes large or it comes in contact with a solid boundary, the cells may become too distorted and of such poor quality that the solver either diverges or encounters a floating point exception condition. In such cases the Java macro executes a computationally demanding remeshing of the whole domain. The time step of calculations is selected such that full domain remeshing is avoided in the initial steps. Once a CFD time step  $\delta t_f$  is converged, the pressure is mapped from the CFD mesh on the rocks to the CSM mesh and exported to file. The Java macro as well as the STAR-CCM+ solver are stopped. Next an LS-DYNA simulation is performed for  $m$  shorter time steps,  $\delta t_s$ , such that  $m \delta t_s = \delta t_f$ , the length of the coupling step. The resulting displacement vectors from LS-DYNA is extracted and translated to NASTRAN format so that they can be imported into STAR-CCM+ for the next step. After this the whole loop is repeated until the termination time.

Using commercial software, as oppose to research software, has many advantages, the primary one being a large industrial user base engaged in using it successfully to solve problems on a daily basis, and consequently computed results are very reliable within the accuracy of the physics models used. Vendors responding to the needs of industry also implement a wide array of physics models, methods to solve a variety of moving mesh problems, and advanced solver algorithms. They normally provide a means for users to add new physics models in the form of user defined subroutines or functions. As such, they provide an excellent foundation for building models to solve new problems, or analyze classic problems using advanced analysis techniques. One disadvantage of using commercial software is that the users do not normally have direct access to the source code and therefore cannot make even minor modifications outside of the means provided by the vendor that might be needed for a new model development. That confines the user to the set of models and tools developed solely by the code owner that can be used when solving an engineering problem. The current implementation of coupling between STAR-CCM+ and LS-DYNA allows for capturing the main effects of rock motion, however, when domain remeshing occurs the information about the motion of a rock from step  $n-1$  to step  $n$  is lost, and the grid fluxes are not included in the momentum equations immediately after remeshing. As a result, the reduction in drag due to acceleration of a rock is not fully accounted for, and rock motion with large displacements will occur at lower velocity difference between the rock and mean flow. The error in this case is conservative in the sense that it would lead to oversizing the riprap for a particular application. Maintaining accurate computation of the pressure on a moving fluid solid interface is important in many FSI applications. The latest 8.04 release of STAR-CCM+ has a new capability: overlapping, overset meshes that may eliminate the need for remeshing when objects in the domain undergo large displacements or contact each other. The next step in the development of STAR-CCM+ and LS-DYNA coupling for FSI analysis will be implementation and testing of overset meshes, which will be described in the upcoming quarter.

Somewhat more complex geometry of the river bed was developed to test the current coupling methodology, than the previously described layouts. The new layout allowed for comparison with Laursen's and Neill's equations for critical velocities [3] frequently used in calculating the motion threshold for riprap. Previously developed shapes of the rocks were used in building new configurations as shown in Figure 2.11. Two layouts were considered in this analysis, layout 1, plain – in figure b and layout 2, with abutment – figure c. The grey rocks in the figures represent stationary rocks; these cannot move in the simulations as the FSI coupling was not activated for them. The three colored rocks in Figure 6b labeled rock 1, rock 2, and rock 3 can move and interact with other boundaries and among themselves through contact algorithms enabled in LS-DYNA. Rock 1 and rock 2 have exactly the same shape as the originally scanned rock. Rock 3 is bigger and more round than the other two but its longest internal measurement is the same, approximately 0.2 m (8 in). Rock 1 is placed flush with the other rocks in the bed. Rock 2 is placed quite deep under the top surface. Rock 3 is sticking out slightly above the bed. The shape of the rocks and their layout influences when they will be picked up and moved by the flow. Placing the rocks at different locations ensures that each of them will have a different critical velocity determined by the detailed geometry and flow field computed in the simulation.

A CFD domain was built with dimensions: 5.0 m long, 1.2 m wide, and 0.65 m high in the recessed area containing the rocks of the riprap layer. The height of the water from the top to the riprap bed top surface was approximately 0.35 m. The size of the domain was designed to be small to conserve computational resources and provide fast turnaround times during development and testing of the coupling procedures. A single phase rigid lid model of the channel flow was also used to keep the model as simple and fast running as possible.

The right end of the domain was set as velocity inlet. The initial water velocity in the domain and the velocity at the inlet was a variable parameter that was manually changed from 2.0 to 3.0 m/s in 0.5 m/s intervals. The sides of the domain were set as symmetry planes. The right side of the model was set as an outflow boundary. In layout 2, with the abutment, the abutment is a wall boundary and the approach flow boundary on the abutment side of the domain was also set as wall boundary. The opposite side is set as a symmetry plane. The domain was meshed using hexahedral cells with varying cell size from 0.004 m (0.16 in) around the rocks up to 0.06 m (2.4 in) away from the rocks and other boundaries. The total count of cells in the model varied between 1.5 million up to 2.0 million cells depending on the layout (plain or abutment) and the evolving position of rocks during the simulation. A  $k-\varepsilon$  turbulence model with Reynolds-Averaged Navier Stokes equations was used to solve for the flow field. An implicit unsteady solver with time step of 0.01 sec was used in the flow solver. That was also the coupling time step i.e. the rate at which data between the CFD and CSM solvers was exchanged.

In LS-DYNA the rocks were modeled as rigid bodies with a density of 2.9 metric tons/m<sup>3</sup> corresponding to granite. The mass of rock 1 and the rock 2 was 4.1 kg (9.0 lb) and the mass of the rock 3 was 7.1 kg (15.6 lb). Three contact definitions were incorporated in the model: (i) among the moving rocks, (ii) between the moving rocks and the stationary rocks and (iii) between the moving rocks and the boundaries. It is sometimes advantageous in LS-DYNA to wrap solid bodies with null, massless shell elements to have more flexibility in defining the contact properties. One of advantages of such an approach in this case is the existence of a non-zero thickness layer around the rocks that prevents them from coming into a full contact in STAR-CCM+. Using this method prevents morphed cells in a near

contact zone from being squeezed to near zero volume and causing flow acceleration to unrealistically high velocities in crevices. The time step of calculations in the LS-DYNA explicit solver was set to  $4.5 \times 10^{-6}$  sec. Use of the explicit solver and such a small time step was needed to stabilize the contact forces between rocks colliding with other rocks or wall boundaries. A time step that is too large can cause excessive contact forces and abnormal behavior of the rocks. Once the STAR-CCM+ and LS-DYNA models were initialized, the coupling between them was activated.

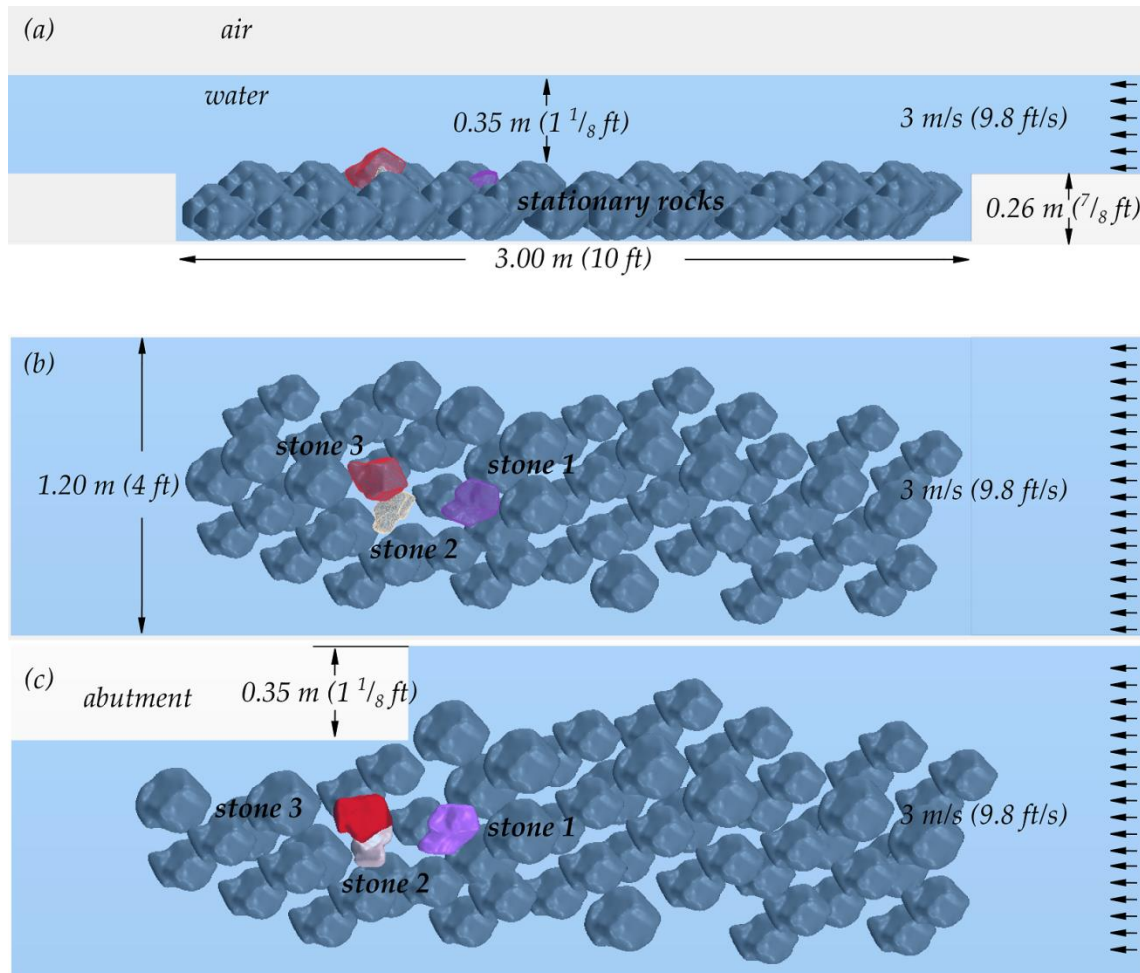


Figure 2.11 Geometry of the CFD model (a) layout 1, side view (b) layout 1, top view (c) layout 2, top view

Approximate values for critical velocity of the modeled rocks can be found by using Neill and Laursen equations [3]. Laursen's formula is given by equation 2.1:

$$V_{CL} = K_U y_2^{1/6} D_{50}^{1/3} \quad 2.1$$

Where:

$K_U$  - is 6.19 for SI units or 11.7 for US customary units,

$y_2$  - is equilibrium scour flow depth (m or ft),

$D_{50}$  - is sediment size (m or ft).

For larger sediment sizes, above 0.03 m (0.1 ft), Neill's formula for critical velocity is defined by equation 2.2:

$$V_{CN} = 11.5 K_U y_2^{1/6} D_{50}^{1/3} \quad 2.2$$

Where:

$K_U$  - is 0.55217 for SI units or 1 for US customary units.

Taking  $y_2 = 0.35$  m,  $D_{50} = 0.24$  m, the critical velocities can be estimated around:  $V_{CN} = 3.31$  m/s (10.8 ft/s) and  $V_{CL} = 3.23$  m/s (10.6 ft/s). Based on that information, simulations were run with an inlet velocity of 2.0 m/s and increased by 0.5 m/s until a large displacement of a rock was observed. The results regarding the detection of motion of the rocks in specific runs are listed in Table 1. For both layout 1 and 2, at an inlet velocity of 2.0 m/s there was no significant motion of the rocks. For both layout 1 and 2 and an inlet velocity 2.5 m/s a local motion of the rock 3 (the largest and most exposed to the flow) was noticeable, but it was not moved out of its position. For layout 1 and an inlet velocity of 3.0 m/s, rock 1 was lifted out of position and moved into the downstream. Rock 2 also started to move locally. Snapshots from that simulation are shown in Figure 7. The fixed-in-place rocks were removed from the view for easier viewing of the moving rocks. A semi-transparent cross section through the domain showing the velocity distribution in the water is also shown in the figure. Snapshots of rocks from the simulation with layout 2 and inlet velocity of 3.0 m/s are shown in Figure 8.

**Table 2.3 Motion of the Rocks in a Specific Analyzed Case**

<b>inlet velocity</b>	<b>layout 1</b>	<b>layout 2</b>
<b>2.0 m/s</b>	no motion	no motion
<b>2.5 m/s</b>	local motion of rock 3	local motion of rock 3
<b>3.0 m/s</b>	motion of rock 3 and local motion of rock 2	motion of rock 1 and 3

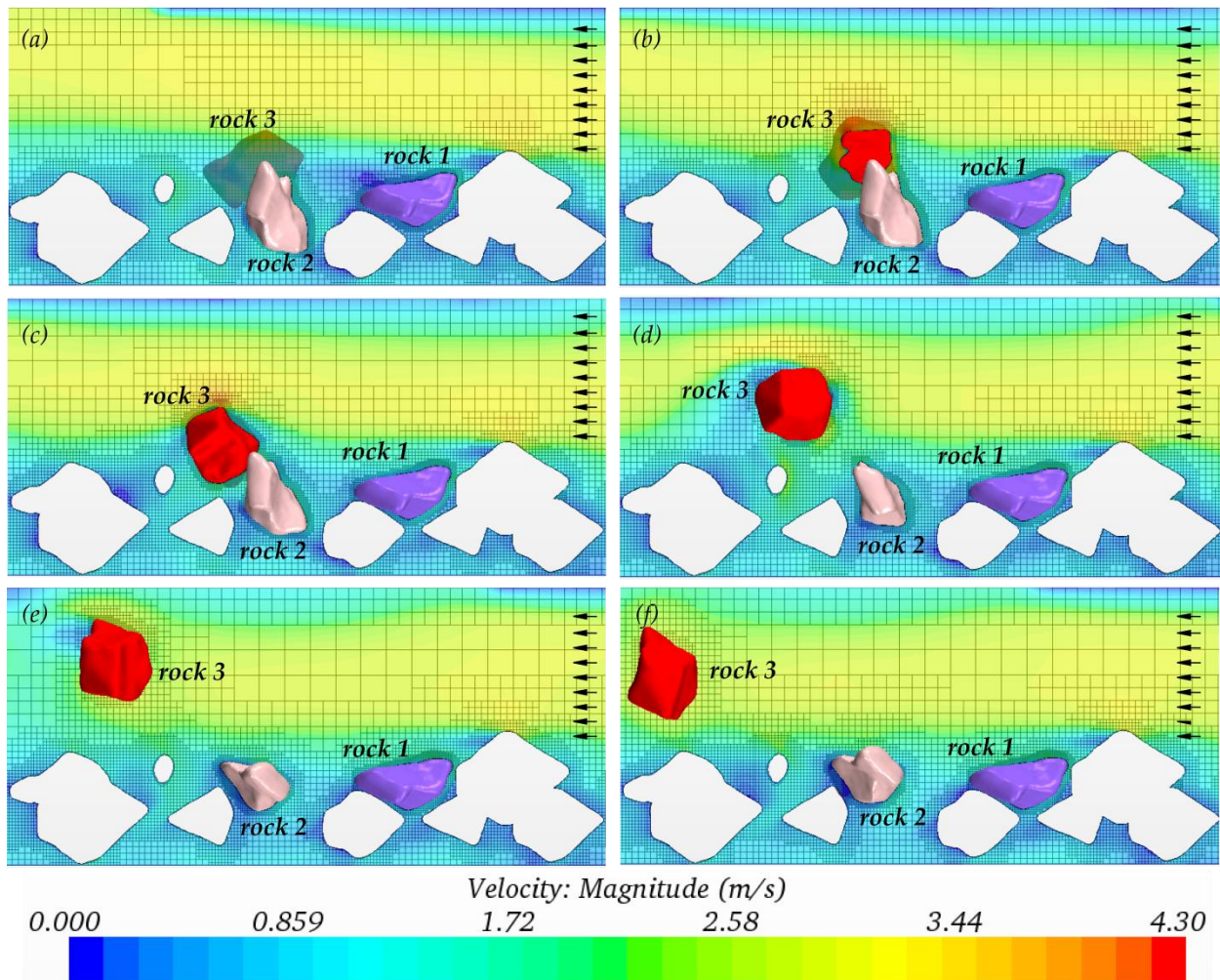


Figure 2.12 Snapshots from simulation for layout 1 and inlet velocity of 3.0 m/s

Procedures were developed to couple STAR-CCM+ CFD software and LS-DYNA CSM software to solve fluid structure interaction problems. The procedures include automated mapping and data exchange of the interface coupling conditions between the two software solvers. An automated recovery from mesh morphing errors that naturally arise when rocks approach contact with solid surfaces was successfully implemented. Two test cases were run and demonstrated that the analysis can be carried out with reasonable use of TRACC cluster resources within a day for a domain residence time of about 2 seconds. The method is ready to be applied to the analysis of incipient motion of riprap at a variety of bridge structures, bed geometries, and flow conditions.

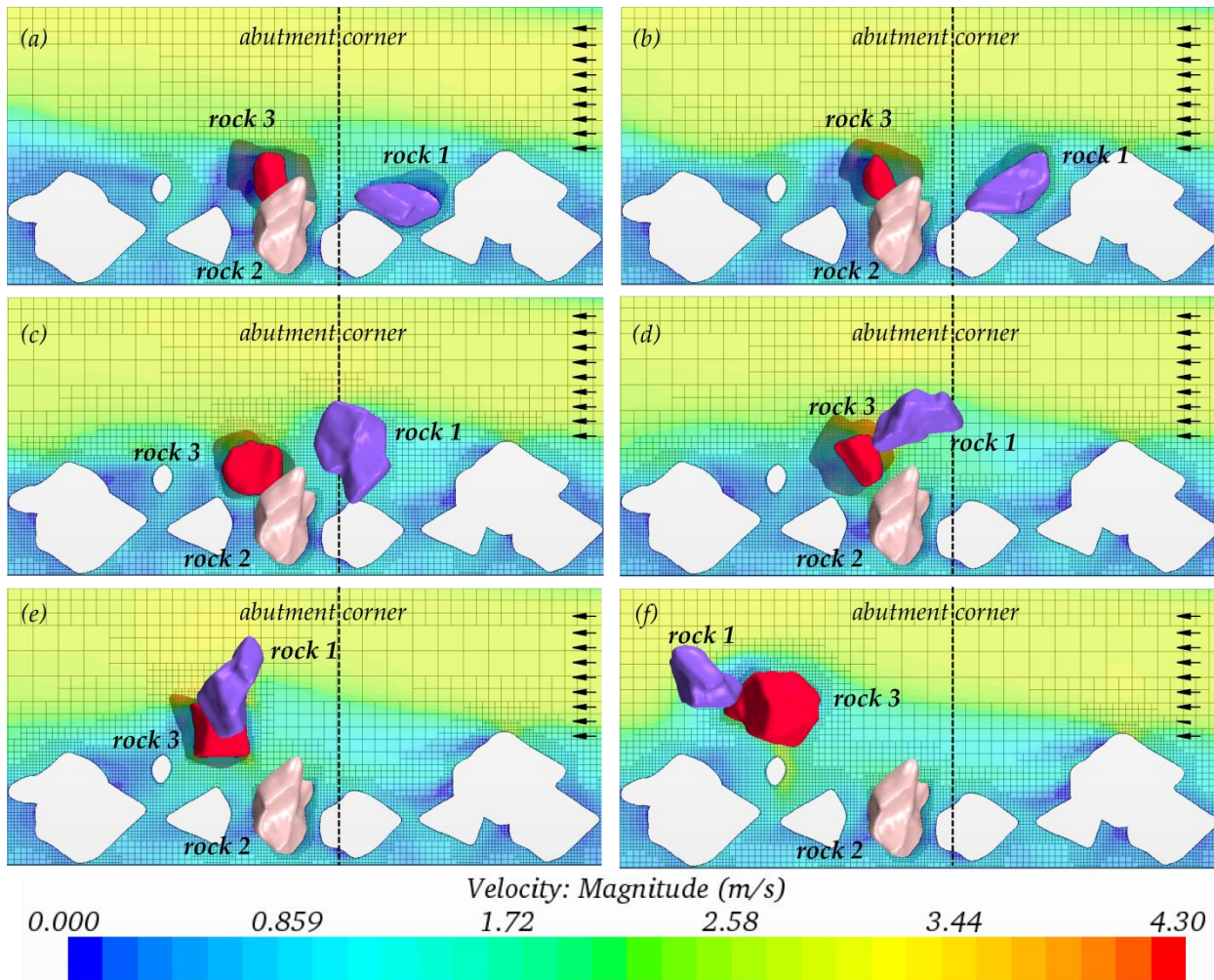


Figure 2.13 Snapshots from simulation for layout 2 and inlet velocity of 3.0 m/s

- [1] CD-Adapco User Guide STAR-CCM+ Version 8.02, 2013.
- [2] Livermore Software Technology Corporation (LSTC), Incompressible fluid solver in LS-DYNA, LSTC, 2013.
- [3] Kerenyi K., Jones J., Stein S., Bottomless Culvert Scour Study: Phase II Laboratory Report, FHWA-HRT-07-026, U.S. Department of Transportation, 2007.

### 2.3. Composite Manning's n of Fish Passage Culvert at TFHRC

Traditionally, culverts are designed for the capacity required to drain storm water during a design high-flow event. That design does not consider the ease of fish passage or aquatic organism passage on a normal day when flow rate is low. The physical characteristics in the culvert under a low flow condition may create adverse conditions for aquatic organisms to pass through. These may include flow velocity

higher than natural stream, shallow water depth, unnatural debris, etc. In the previous quarters, the research team conducted physical modeling and CFD modeling to characterize the flow conditions with various flow velocities, depths, and embedments of corrugated metal pipes pertaining to their qualification for fish passage. The modeling was done with several given discharge rates for every pipe geometry, flow depth, and embedment. The method to obtain the flow rates used in the modeling with given pipe slope and other relevant parameters was not discussed. One of the necessary parameters to obtain the discharge rate is the Manning's  $n$  value. This parameter varies with the roughness of the pipe, particle size of bedding material, and the geometry of the cross-section of the flow. The  $n$  value that can be used to calculate discharge rate is a composite result of various influences from the bedding material and pipe roughness. In this quarter, a method for evaluation of the composite Manning's  $n$  is studied. CFD analysis is used to develop a formula to calculate the composite Manning's  $n$ . This section explains how to obtain the composite roughness using STARCCM+.

The force equilibrium equation for a typical culvert pipe shown in Figure 2.14 is as follows,

$$\tau_w A_p = \Delta p A \quad 2.5.1$$

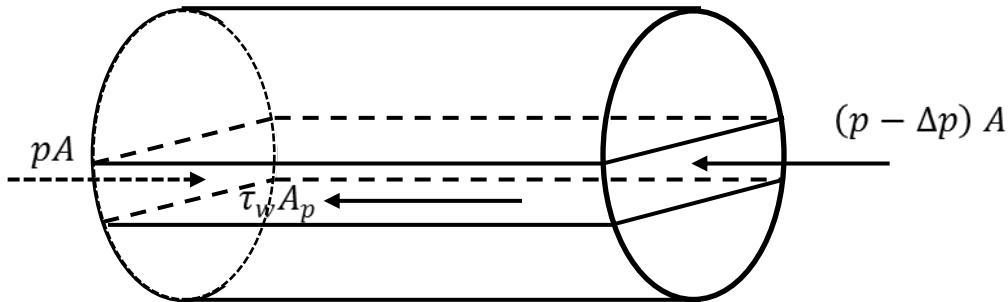


**Figure 2.14 Force Analysis Sketch on the Culvert Pipe**

where  $\tau_w$  is the average shear stress on the bed and pipe wall.  $A_p$  is the wetted area in culvert pipe.

The average shear stress can be calculated using Eq. 2.5.2 and Eq. 2.5.3 for a given friction coefficient,  $f$ ,

$$\tau_w = \frac{f}{8} \rho V^2 \quad 2.5.2$$

$$f = f \left( Re, \frac{\delta}{R_H} \right) \quad 2.5.3$$

where  $f$  is friction coefficient and  $\delta$  is the composite roughness height of culvert combining the effect from the particle size of the gravel bed and the corrugation height of the pipe wall, defined as:

$$\delta = \frac{l_b}{l_p} D_{50} + \frac{l_w}{l_p} \Delta \quad 2.5.4$$

where  $\Delta$  is the corrugation height,  $l_p$  is the wet perimeter,  $l_b$  is the width of the gravel bed, and  $l_w$  is the length of side wall, as shown in Figure 2.15.  $Re$  is Reynolds number, defined as  $Re = \frac{\rho V R_H}{\mu}$ .

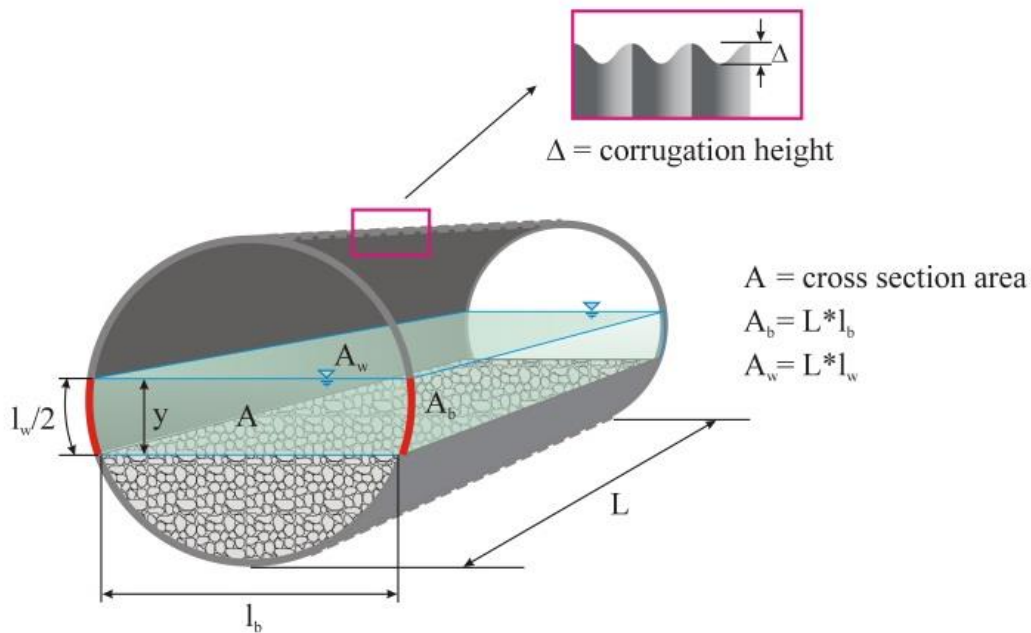


**Figure 2.15 Geometrical Parameters of Culvert**

Given a flow condition, the average shear stress  $\tau_w$  can be found from the pressure drop between the inlet and outlet using CFD analysis with a periodic boundary condition to determine the pressure drop through a section of pipe under fully developed flow conditions using equation 2.5.1. The value of  $f$  can then be obtained from equation 2.5.2. According to the Chezy, Manning, and Darcy formulas, the composite Manning coefficient is written as:

$$n = \sqrt{\frac{f}{8g}} R_H^{\frac{1}{6}} \quad 2.5.5$$

Equation 2.5.5 can be used to get a composite roughness from CFD results for specified flow conditions. Uniformly distributed spheres with diameter of  $D_{50}$  are created in CFD modeling as shown Figure 2.16 to simulate the roughness of the gravel, while the additional roughness from the corrugation is included in the model since the precise geometry of the corrugated wall is modeled.

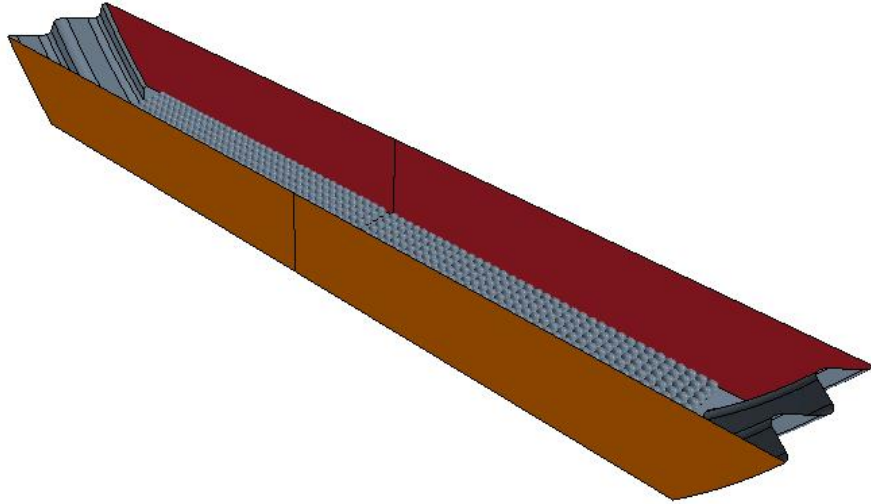


**Figure 2.16 Geometrical Model with Uniform Bed Roughness of  $D_{50}$**

The pressure difference between the inlet and outlet of a periodic boundary condition model can be calculated using a surface average function in STARCCM+. The pressure on the inlet plane and outlet plane are shown in Figure 2.17. The convergence of the difference in average pressure through the iteration process is shown in Figure 2.18. This pressure difference can be represented by a uniform equivalent shear stress throughout the wetted perimeter by Equation (2.5.1). The Manning's  $n$  value can then be obtained from equations 2.5.2 and 2.5.5.

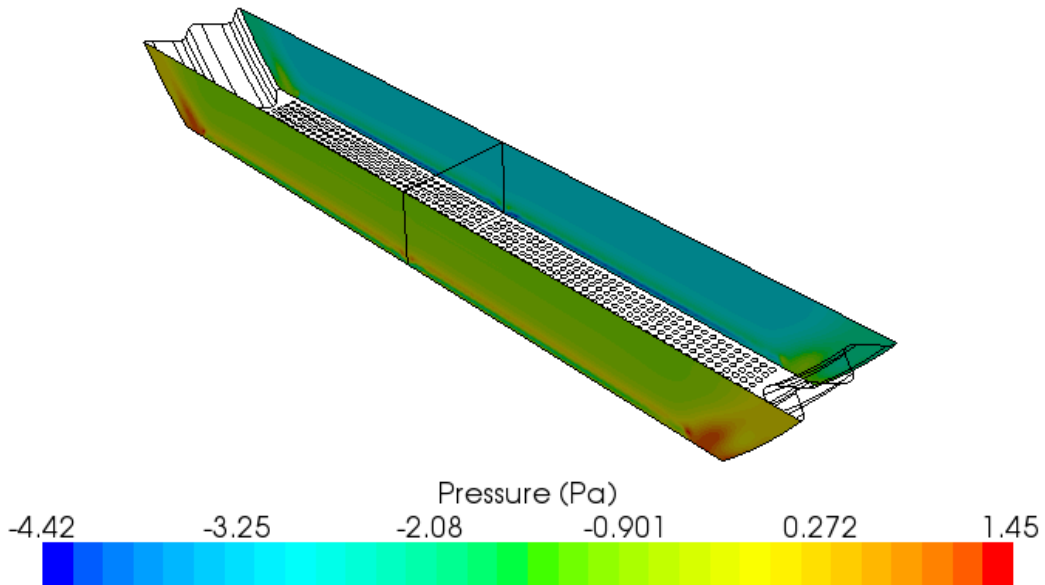


**Figure 2.17 Pressure distribution on two planes with periodic boundary**

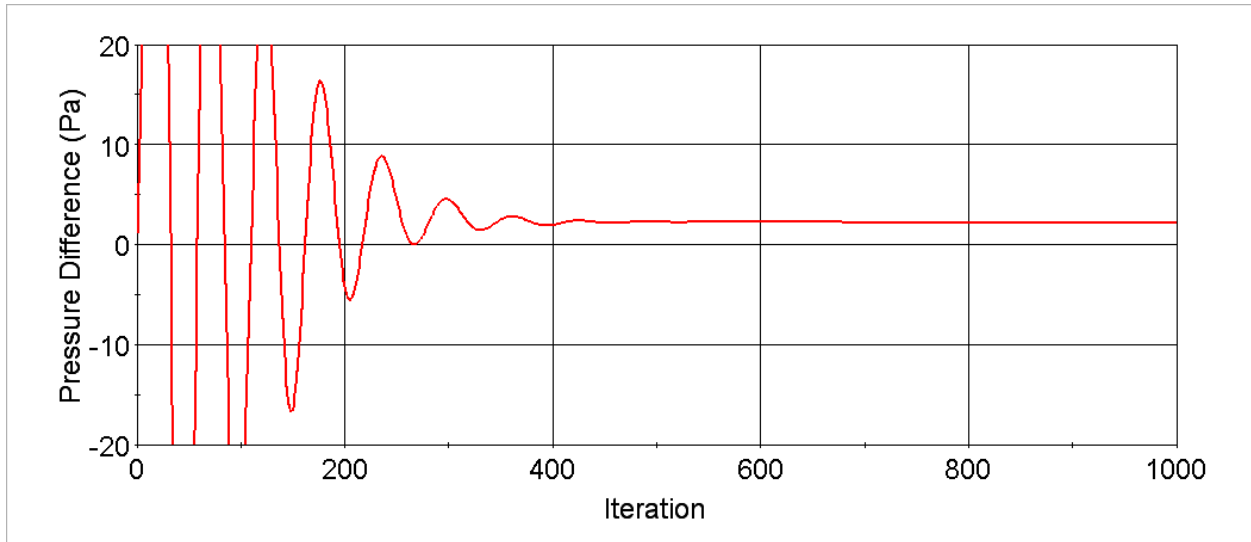


**Figure 2.18 Pressure difference monitor between two planes with periodic boundaries**

Figure 2.19 and Figure 2.20 show the typical velocity distribution in the culvert longitudinal direction.

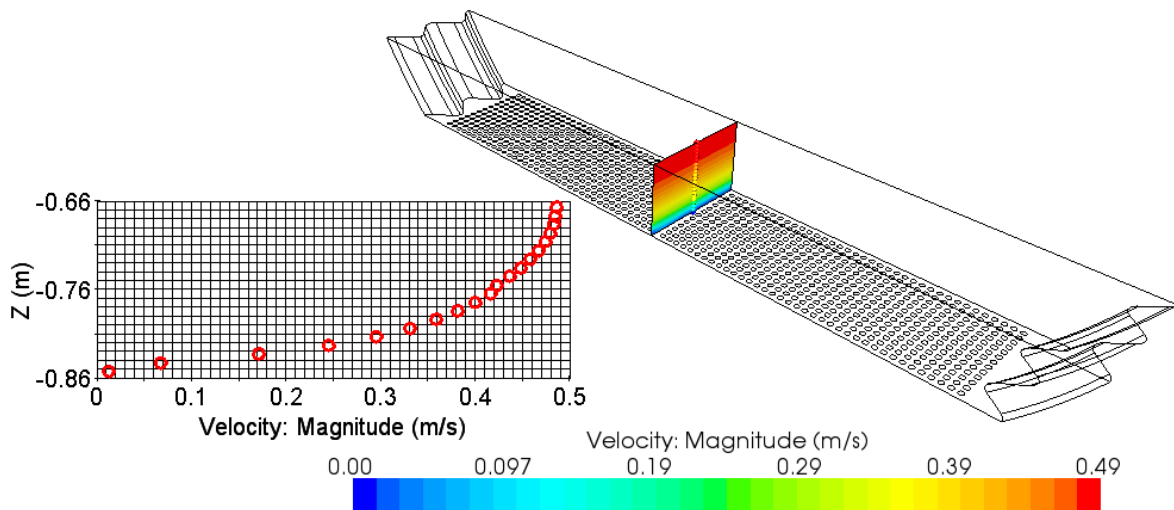


**Figure 2.19 Velocity magnitude distribution**

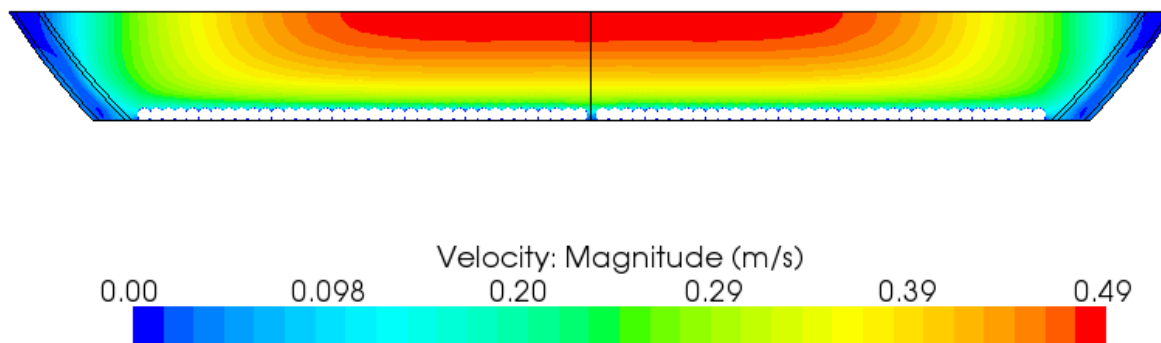


**Figure 2.20 Velocity Magnitude Distribution on the Cross Section**

The CFD analysis results for a culvert with an 8 ft diameter show that the composite Manning coefficient is independent upon Reynolds number within the testing range of velocity, 1 – 3 ft /s Reynolds number range of  $0.5-3.6 \times 10^5$ . It is dependent on the dimensionless parameter  $\frac{\delta}{R_H}$ . An empirical formula can be used to show this relationship:

$$n = 0.1248 \frac{\delta}{R_H} + 0.012 \quad 2.5.6$$

where  $\delta$  can be obtained from equation 2.5.4. This formulation makes it possible to calculate a composite n value from the pipe geometry, embedment, and particle size. The calculation would involve an iteration process because the lengths used in equation 2.5.4 are functions of depth, which may not be known before an n value is given. A user of these equations may start by guessing one of the parameters (such as n), then go through open channel flow formulas (Manning's equation, continuity) and equation 2.5.6 to find an adjustment to the guessed parameter until it's consistent with the previous guess. This is essentially a fixed point iteration that can be carried out in a spread sheet.

Figure 2.21 shows the analysis of regression between Manning's n and  $\ln(\text{Re})$  indicating that Manning's n is independent on Reynolds number in the low flow condition. Figure 2.22 illustrates the linear regression between Manning's n and the composite roughness height  $\delta/R_H$ .

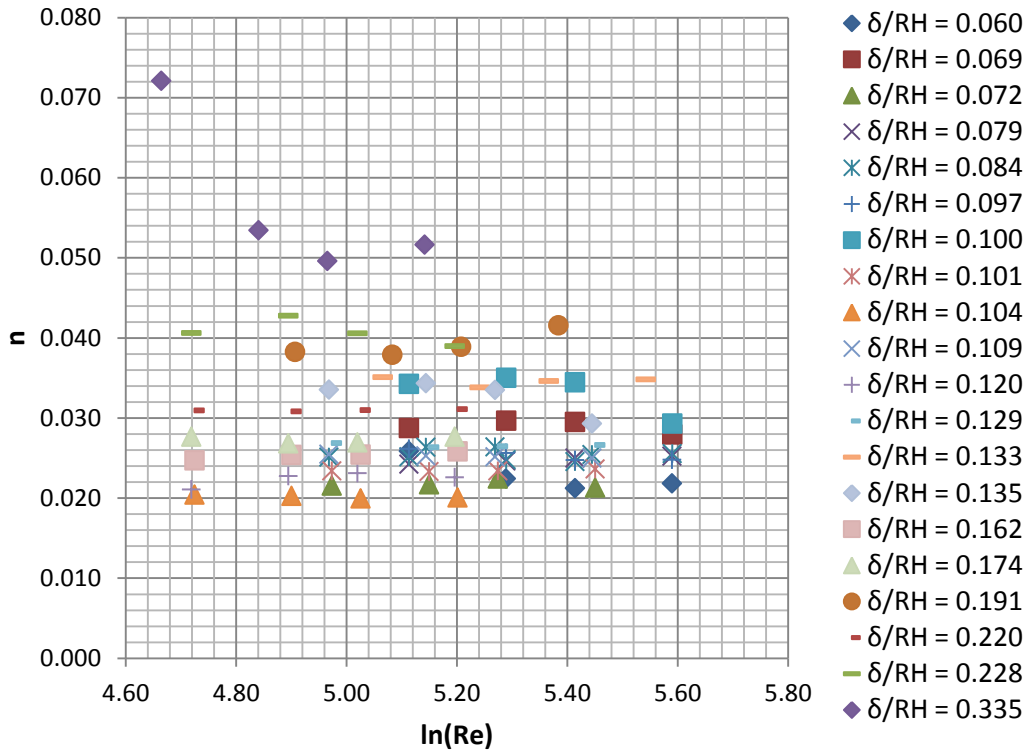


Figure 2.21 Analysis of Repression between Manning'n and lg(Re)

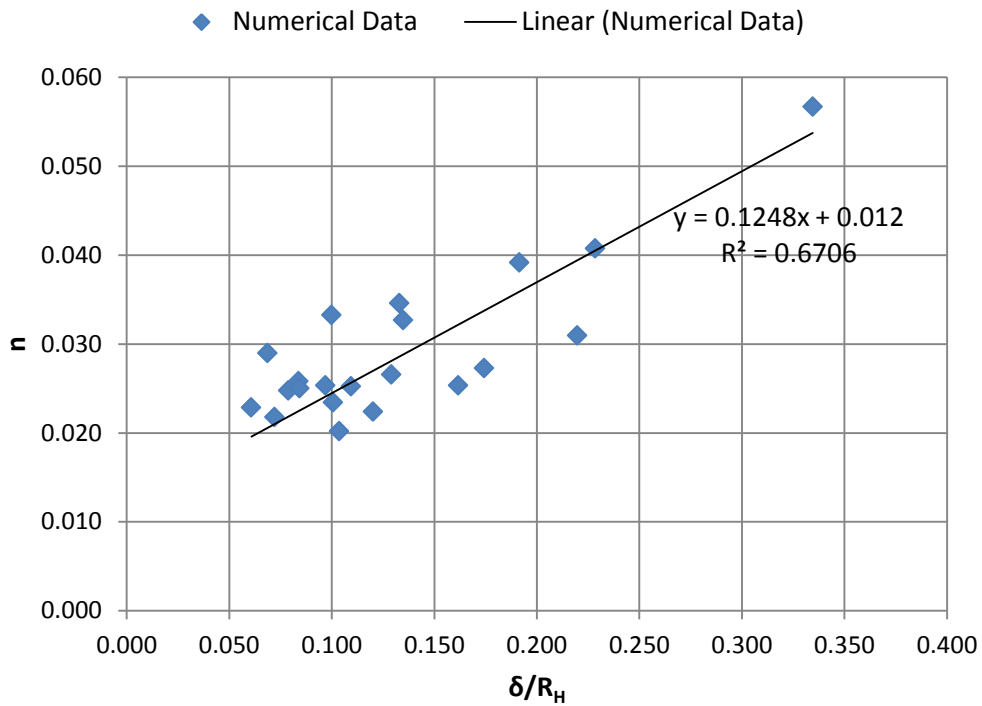


Figure 2.22 Linear Regression between Manning'n and  $\delta/R_H$

## **3. Wind Engineering Modeling and Analysis**

### **3.1. Drag and Lift on Variable Message Signs under Conditions with Wind**

#### **3.1.1. Model Development**

In the previous quarters attempts were made to classify sign vibrations as a result of truck initiated wind impulses. Star-CCM+ models were coupled with LS-DYNA in hopes of capturing complex fluid structure interactions. Although minor structural vibrations and associated displacements were noted, large scale movements were not found within the simulation analysis. First hand reports claimed message signs motions on the order of a foot and more due to passing trucks underneath the sign. However, one way and two way coupled simulations did not indicate vibrations with the amplitudes greater than a couple of inches. This finding is consistent with a general classification of wind effects on VMS structures to aerodynamic and aeroelastic. Natural and truck-induced wind gusts are classified as aerodynamic effects which are due solely to external loading. Aeorelastic effects are due to the interaction of aerodynamic forces and structural motion, that is, motion of the structure affects the aerodynamic force acting on it.

The previously obtained numerical results indicate that the observed in the field vibration of the VMS could have been due to either wind galloping that was triggered or amplified by the truck-induced gusts.

At the request of TFHRC, additional rigid body simulations were performed on rotated signs to better classify the forces associated with shifting wind patterns. This shifting of wind direction was thought to provide a better environment for galloping. Models were developed from previous tests (see Figure 3.1) and the sign geometry was rotated about both vertical (Y-Axis) and horizontal (Z-Axis) directions. During simulations force and lift coefficients, as a function of time, were monitored to judge convergence.

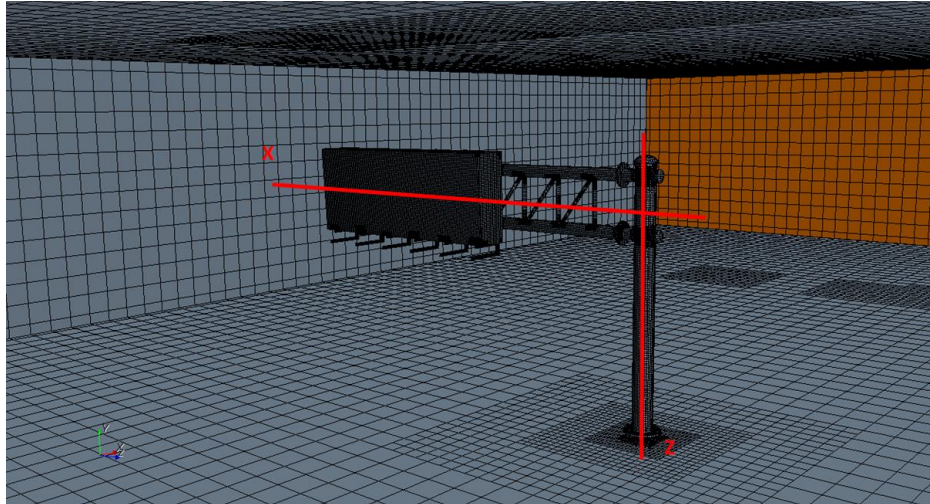


**Figure 3.1 Initial Sign Geometry**

A representative air speed of 8.94 m/s (20 mph) was chosen for all conducted simulations. In addition to the rotation analysis, a mesh sensitivity study was performed to justify mesh parameters. Within the meshing scheme a decision had to be made on the mesh orientation. Within a hexahedral meshing scheme cells can be orientated in specified directions. For general best practices within CFD cells should be aligned with the flow field. However, because the sign was to be rotated meshing could then be orientated either: with the inlet flow or with the flow around the sign as listed in Table 3.1. A meshing study was therefore conducted on three separate mesh configurations to determine the associated alignment error. Two coarse hexahedral meshes and one dense polyhedral mesh used for the grid study.

**Table 3.1 Meshing Schemes**

Mesh No.	Mesh Scheme	Cell Count (Million)	Cell Alignment
1	Hexahedral	1.50	Inlet
2	Hexahedral	1.45	Sign
3	Polyhedral	10.3	-

### 3.1.2. Results

In the analysis conducted by rotating the sign through the horizontal axis a slight drop in the overall force was seen. As the horizontal rotation angle increased the force on the sign consequently decreased due to reduction in sign frontal area. The drag and lift coefficient on a bluff body were calculated in the simulations using the following equations:

$$C_D = \frac{2F_d}{\rho v^2 A_I}; \quad C_L = \frac{2F_L}{\rho v^2 A_{II}}$$

In which  $F_D$  is the fluid drag force on the body,  $F_L$  is the fluid lift force,  $\rho$  is the fluid density,  $v$  is the fluid velocity,  $A_I$  is the body frontal area in the direction of the flow, and  $A_{II}$  is the body area in the direction

perpendicular to the flow. Figure 3.2 presents the change of drag and lift coefficient as functions of angle of attack.

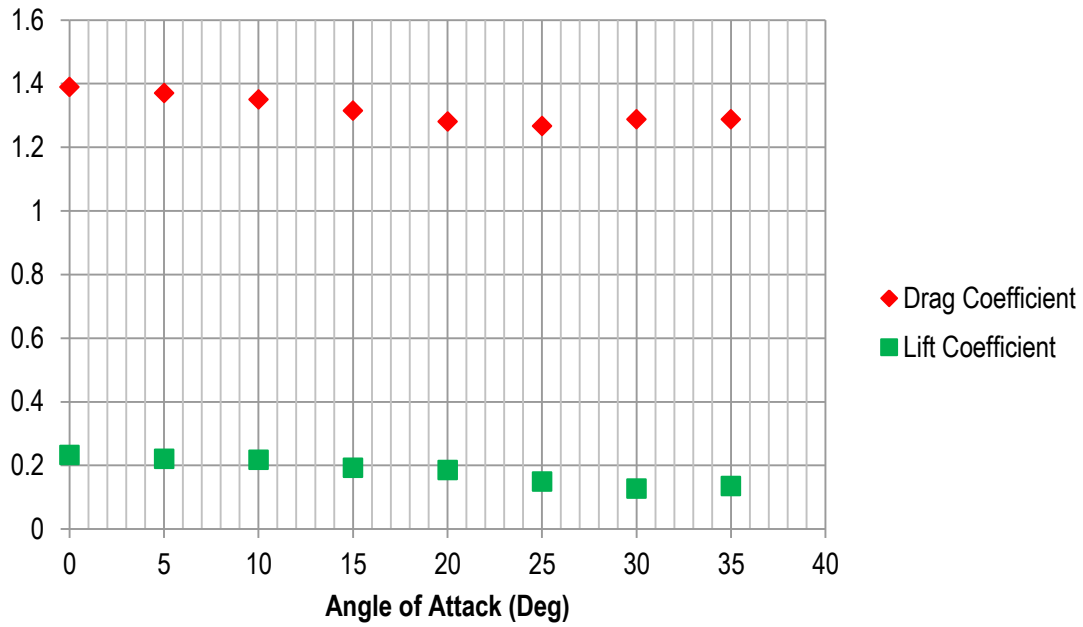


Figure 3.2 Drag and Lift Coefficients As a Function of Y-Axis Anlge of Attack

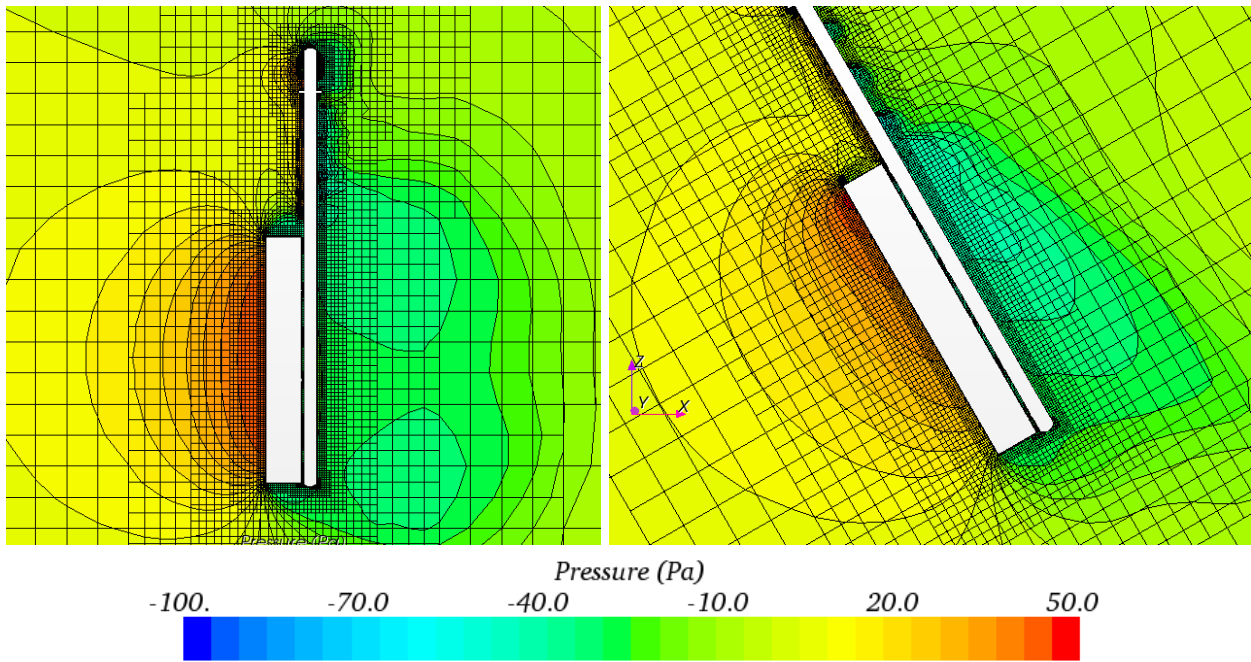


Figure 3.3 Pressure distribution around sign (left) perpendicular to the flow and (right) rotated 30 about Z axis

In the second study where the sign box was rotated about X axis the lift coefficient was changing greatly, from 0.6 to -0.2 as the frontal surface was changing the orientation. The drag coefficient wasn't changing that much. Initial inclination of the frontal surface of the sign was - 4 deg, thus the point at which the lift coefficient was changing sign corresponded to the rotation of 4 deg in the opposite direction. Figure 3.4 shows the lift and drag coefficients as functions of angle of attack. Figure 3.5 shows the two most extreme orientations of the sign box – 10 deg counter clockwise and +5 deg clockwise

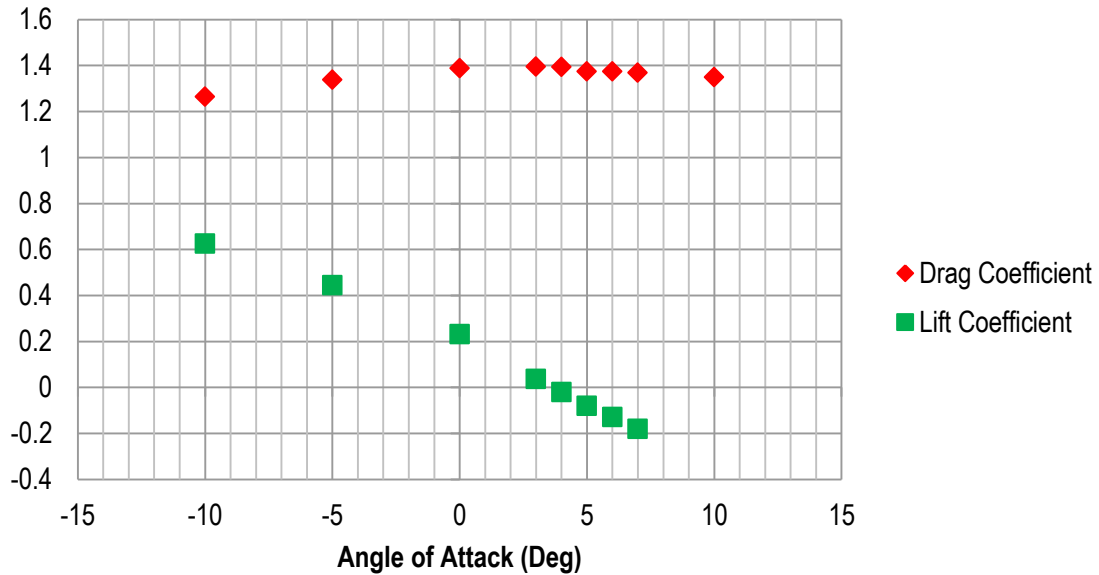


Figure 3.4 Drag and Lift Coefficients as a Function of Z-Axis Angle of Attack

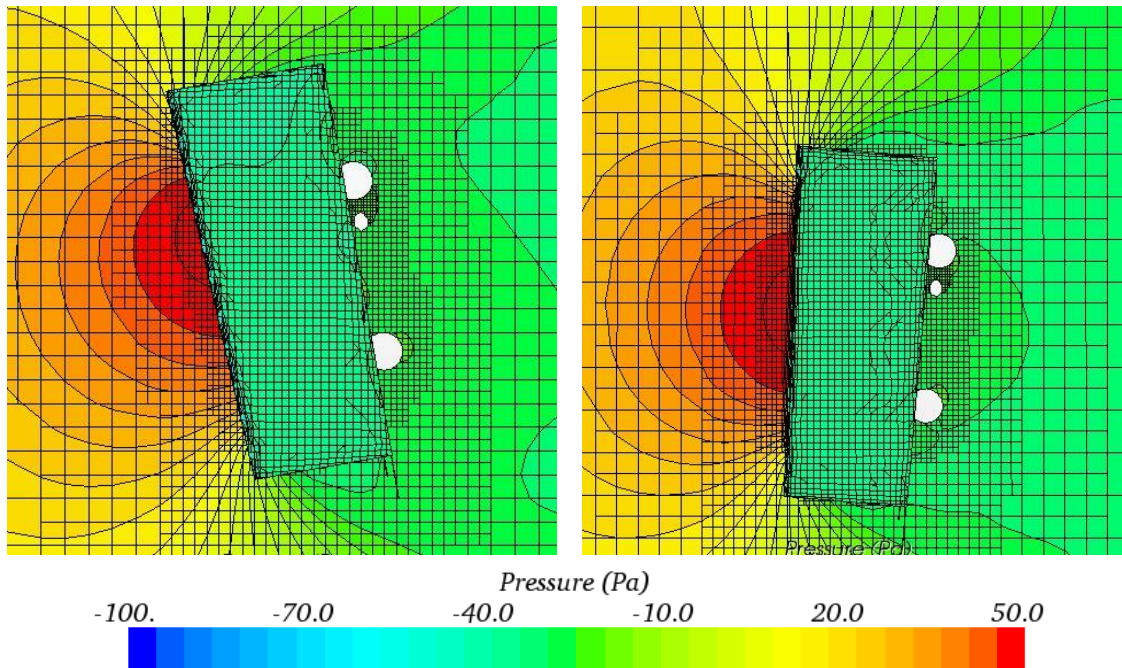
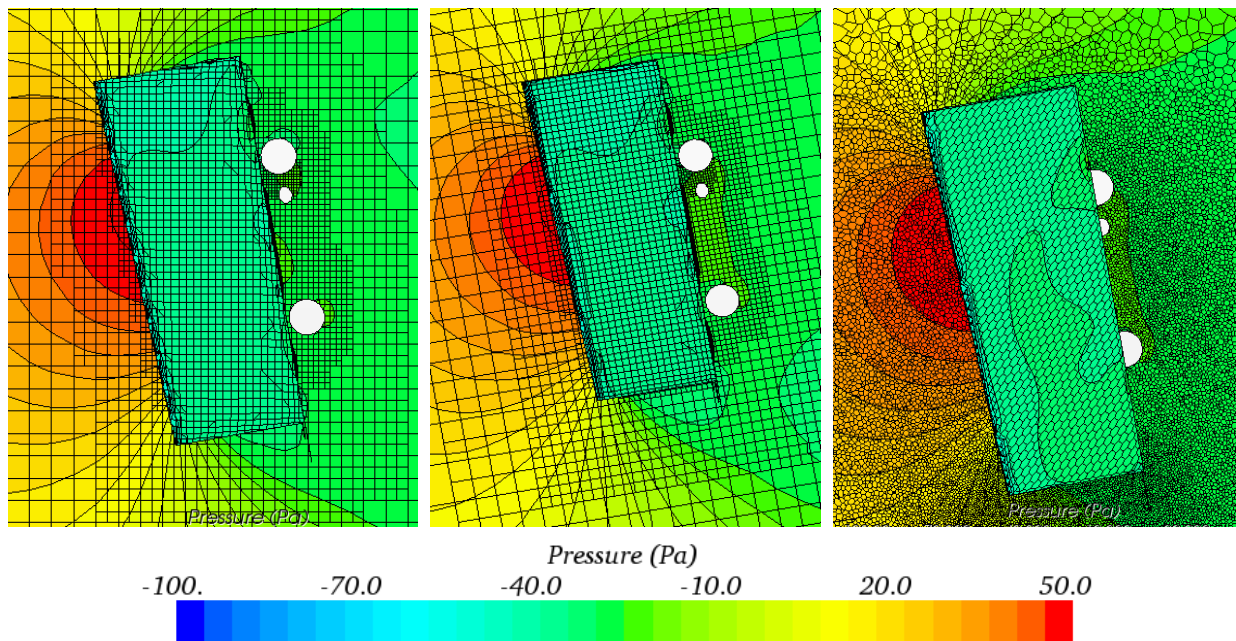


Figure 3.5 Pressure distribution around sign (left) rotated -10 deg (CCW) and (right) +5 deg (CW) about X axis

Within the final portion of the analysis a mesh dependency study was conducted. The purpose of it was to determine what effect the mesh alignment played in the drag and lift coefficient calculations. A representative configuration of a sign rotated negative ten degrees about X axis was chosen as it would show the greatest effect of cell alignment error. Two hexahedral and one polyhedral mesh schemes were studied as shown in Figure 3.6. It was found that the force coefficients differed in the third decimal place within the two studied hexahedral schemes. This was a good indication that cell alignment would not play a significant role in the solution. When using the dense polyhedral mesh the solution deviated from the solution on the first mesh setup by about 2 %. It is safe to assume that for the engineering purposes the mesh alignment does not influence the computations of drag and lift forces on the VMS. The values of lift and drag coefficients in the three described models are presented in Table 3.2.

**Table 3.2 Drag and Lift Coefficients for Each Meshing Scheme**

Mesh No.	Mesh Scheme	Drag Coefficient, $C_D$	Lift Coefficient, $C_L$
1	Hexahedral	1.265	0.627
2	Hexahedral	1.260	0.610
3	Polyhedral	1.243	0.611



**Figure 3.6 Pressure Distribution Around Sign With Mesh Aligned With Flow, three meshing schemes**

### 3.2. Wind Tunnel Model with Neutral Vane Position in Turbulence Generator

In the previous quarter the simulated flow conditions were compared to the measured air velocities in the lab. The air velocity in the model significantly differed from the experimental values. The fan model cage and blade geometry did not match that of the fan in the laboratory and a new model of wind tunnel laboratory without explicitly modeled fan was developed. Instead an inlet boundary was set in the wind tunnel in the front of the first mesh screen. The inlet velocity was increased until the velocity at one point in the testing section matched the experimentally measured velocity. For such model the velocities in several cross sections through the room were compared. Although in such model the velocities matched quite well the measured values there was a significant difference in the returning flow on the left side of the fan, where the turbulence generator is located. In the CFD model the blades of the generator were not set to the neutral position. Instead they were slightly turned blocking the flow and causing the discrepancy. In this quarter the turbulence generator geometry was replaced with a new one where the blades were set to neutral position. The velocity field across the room in the new model is shown in Figure 3.7. It can be noted that the flow through the turbulence generator is now unobstructed.

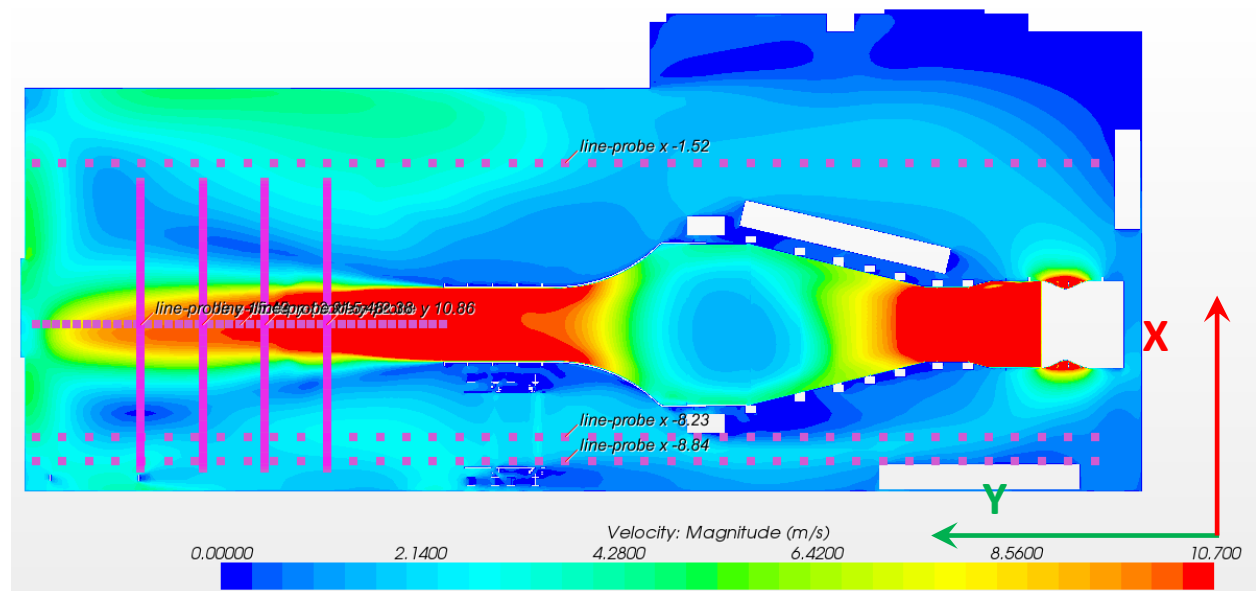


**Figure 3.7 CFD computed velocity field at the height of the laboratory measurements with measurement cross sections**

Figure 3.8 through Figure 3.11 show the comparison between the velocity distributions in the traverse cross sections through the room downstream of the wind tunnel for the previous CFD model, the updated one with turbulence generator in neutral position and the measured values. The biggest improvement can be noted in Figure 3.11. Figure 3.12 and Figure 3.13 show cross sections along constant X coordinates showing the returning flow velocities. The velocity in the cross section near the wall with the turbulence generator matches closer the experimental data. The current model approximates the flow in the wind tunnel lab quite well. Further improvements may pertain to rebuilding the fan model in a more realistic way.

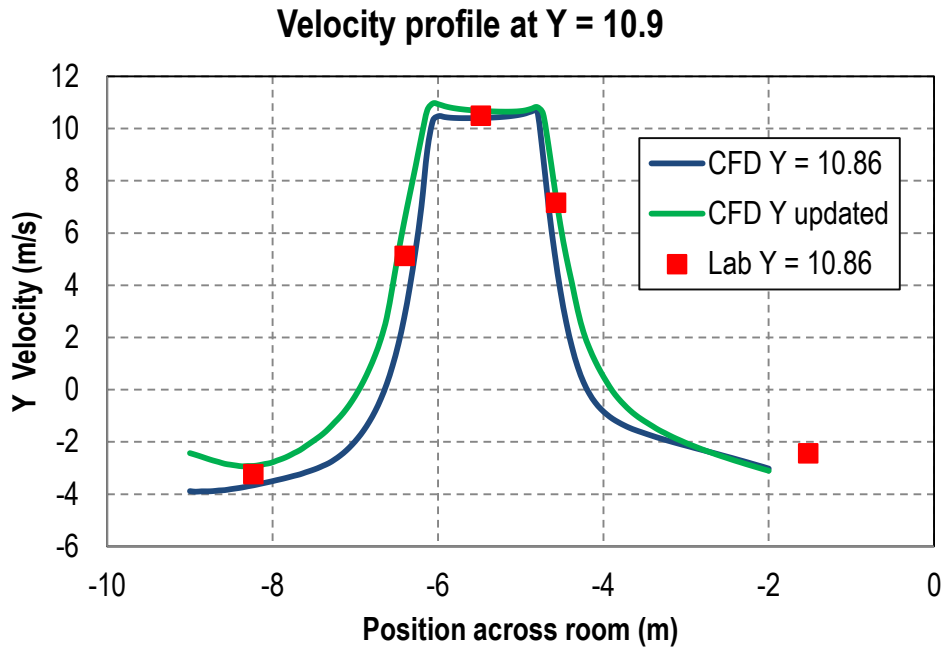


Figure 3.8 Comparison of measured and computed velocity distribution at first column of points that spanned the room

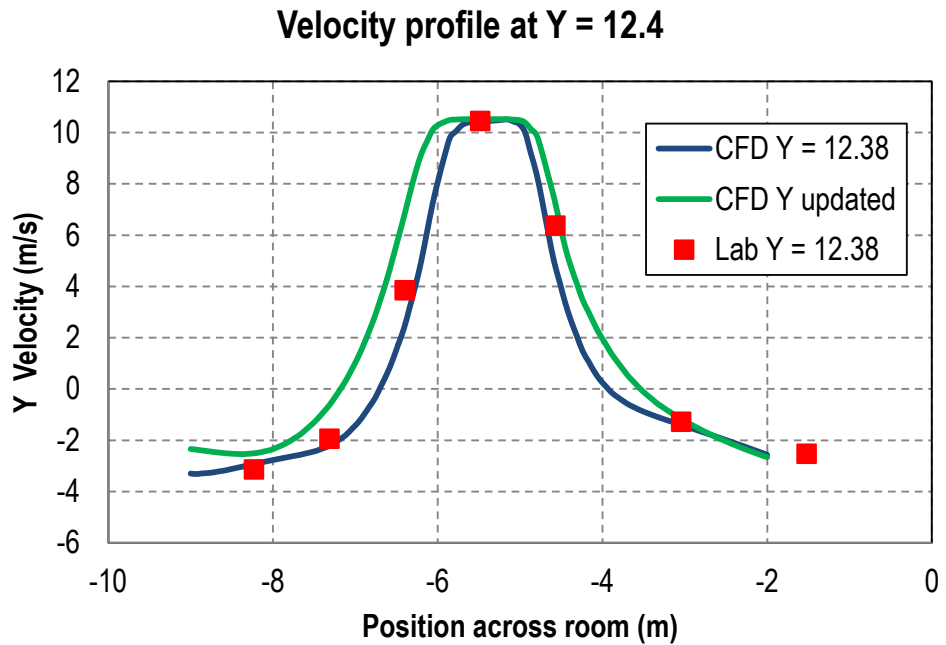


Figure 3.9 Comparison of measured and computed velocity distribution at the second set of measured points spanning the room in the downstream of the wind tunnel jet

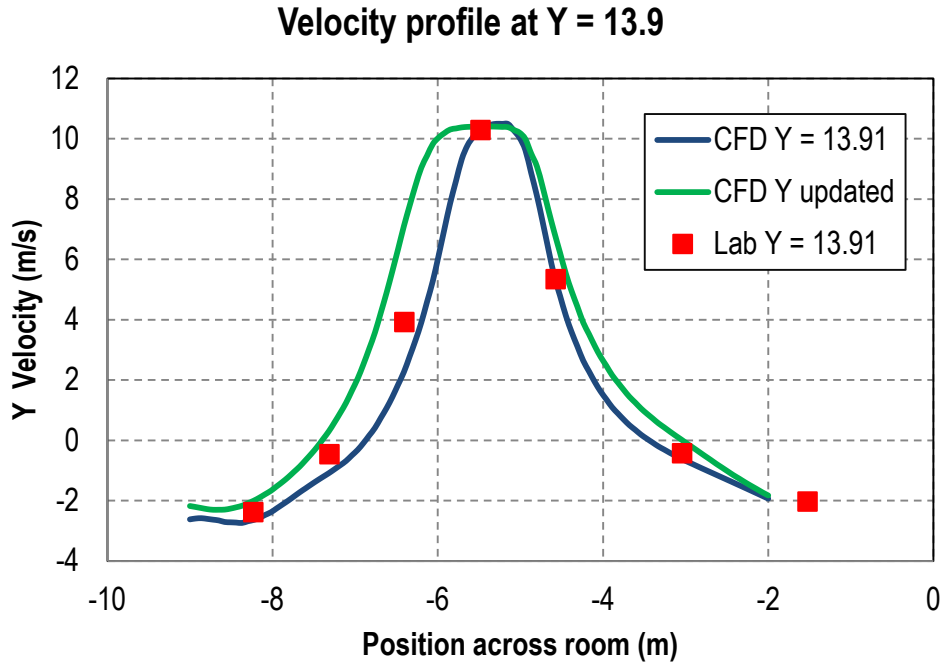


Figure 3.10 Comparison of measured and computed velocity distribution at the third set of measured points spanning the room in the downstream of the wind tunnel jet

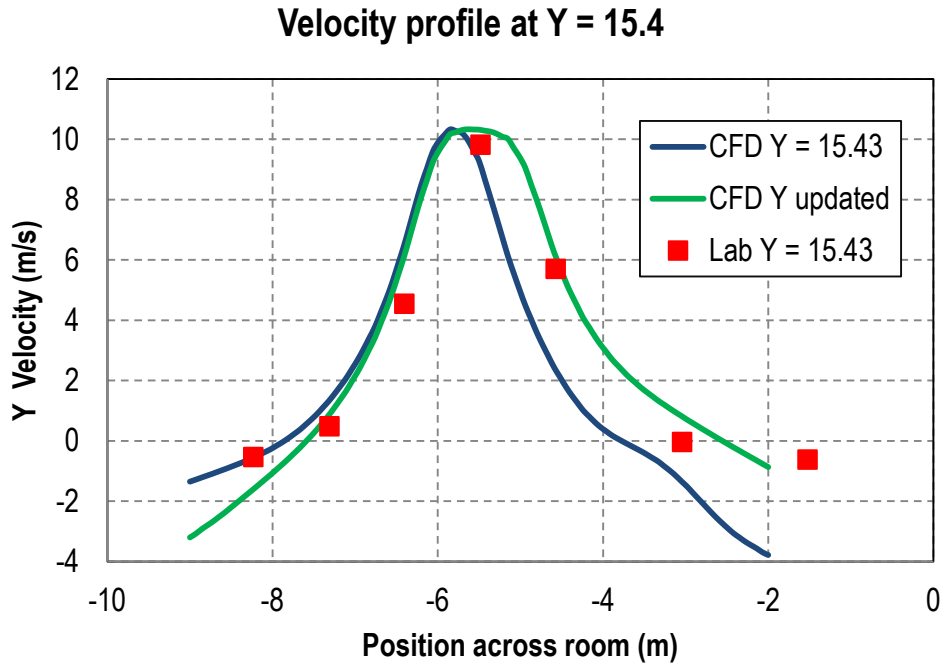


Figure 3.11 Comparison of measured and computed velocity distribution at the fourth set of measured points spanning the room in the downstream of the wind tunnel jet

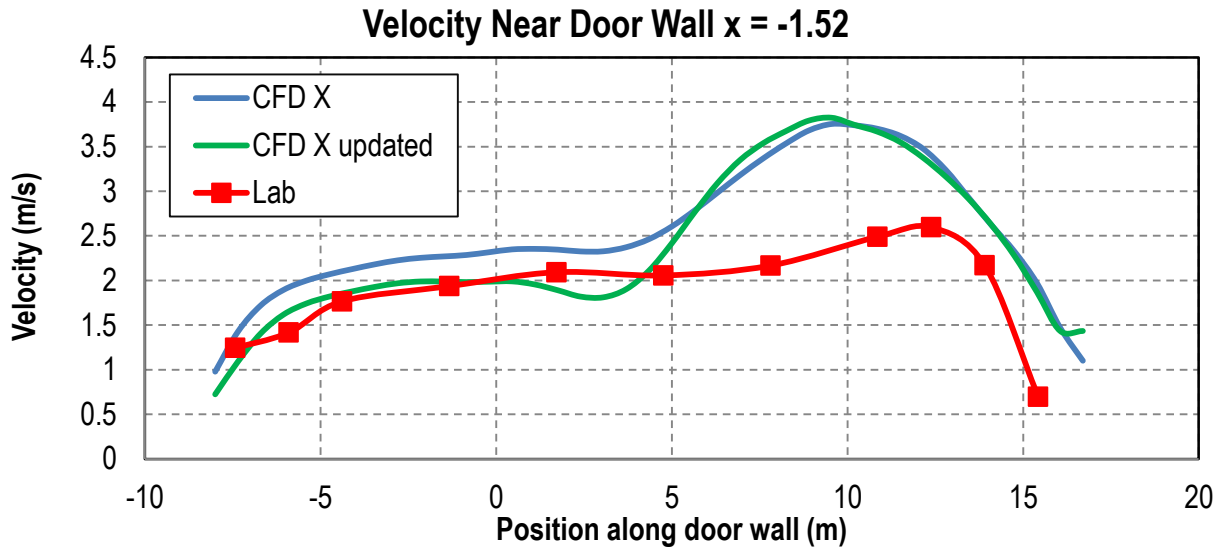


Figure 3.12 Measured and CFD velocity magnitude near the wall with the door

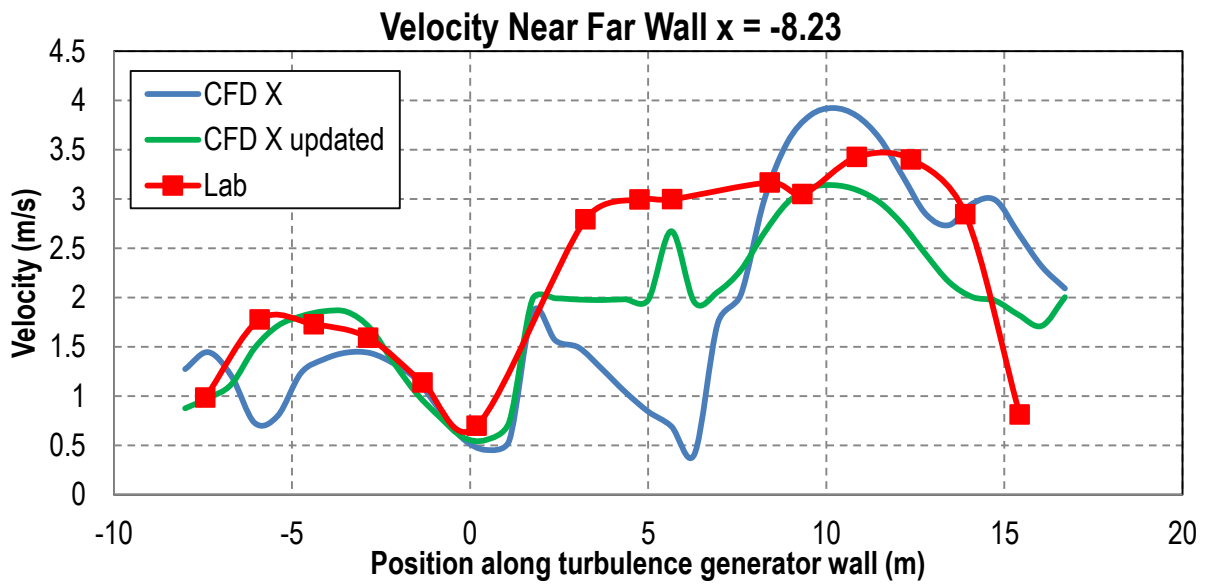


Figure 3.13 Measured and CFD velocity magnitude near the wall with the turbulence generator

#### **4. Technology Transfer and TRACC Facility User Support**

TRACC CFD staff continued CFD collaborator video conferences held every other Thursday morning between TRACC, TFHRC, and other transportation researchers using the TRACC clusters for CFD analysis. Graduate student researchers and occasionally their advising professor at the University of Florida continued to join the sessions to expand their experimental program by adding CFD analysis of their experimental flume. A bridge engineer from California DOT working to apply CFD to practical problems in river hydraulics near bridges for the state was also a regular in the videoconferences. TRACC staff also continued to provide technical support to both new and existing TRACC cluster users.



**Energy Systems Division**  
Argonne National Laboratory  
9700 South Cass Avenue, Bldg. 362  
Argonne, IL 60439-4815

[www.anl.gov](http://www.anl.gov)



Argonne National Laboratory is a U.S. Department of Energy  
laboratory managed by UChicago Argonne, LLC